PLOS BIOLOGY

METHODS AND RESOURCES

Insight into small molecule binding to the neonatal Fc receptor by X-ray crystallography and 100 kHz magic-angle-spinning NMR

Daniel Stöppler[1‡], Alex Macpherson[2‡], Susanne Smith-Penzel[3], Nicolas Basse[4], Fabien Lecomte[2], Hervé Deboves[5], Richard D. Taylor[2], Tim Norman[2], John Porter[6], Lorna C. Waters[7], Marta Westwood[2], Ben Cossins[2], Katharine Cain[8], James White[2], Robert Griffin[2], Christine Prosser[2], Sebastian Kelm[2], Amy H. Sullivan[9], David Fox, III[9], Mark D. Carr[7], Alistair Henry[2], Richard Taylor[2], Beat H. Meier[3], Hartmut Oschkinat[1]*, Alastair D. Lawson[2]*

1 Leibniz-Forschungsinstitut für Molekulare Pharmakologie, Berlin, Germany, **2** UCB Celltech, Slough, United Kingdom, **3** Laboratory of Physical Chemistry, ETH Zürich, Zürich, Switzerland, **4** Sanofi, Strasbourg, France, **5** Evotec, Milton, United Kingdom, **6** Midatech Pharma Plc, Milton, United Kingdom, **7** Leicester Institute of Structural and Chemical Biology, University of Leicester, Leicester, United Kingdom, **8** Vertex, Milton, United Kingdom, **9** Beryllium Discovery, Bedford, Massachusetts, United States of America

‡ These authors share first authorship on this work.
* oschkinat@fmp-berlin.de (HO); alastair.lawson@ucb.com (ADL)

Citation: Stöppler D, Macpherson A, Smith-Penzel S, Basse N, Lecomte F, Deboves H, et al. (2018) Insight into small molecule binding to the neonatal Fc receptor by X-ray crystallography and 100 kHz magic-angle-spinning NMR. PLoS Biol 16(5): e2006192. https://doi.org/10.1371/journal.pbio.2006192

Academic Editor: Ann Stock, UMDNJ/Robert Wood Johnson Medical School, United States of America

Received: February 6, 2018

Accepted: May 2, 2018

Published: May 21, 2018

Data Availability Statement: The crystallographic data are available from the Protein Data Bank (www.rcsb.org, accession numbers 6C97, 6C98, and 6C99) and the chemical-shift data from the Biological Magnetic Resonance Data Bank (www.bmrb.wisc.edu, accession number 27437). All other relevant data are within the paper and its Supporting information files.

Abstract

Aiming at the design of an allosteric modulator of the neonatal Fc receptor (FcRn)–Immunoglobulin G (IgG) interaction, we developed a new methodology including NMR fragment screening, X-ray crystallography, and magic-angle-spinning (MAS) NMR at 100 kHz after sedimentation, exploiting very fast spinning of the nondeuterated soluble 42 kDa receptor construct to obtain resolved proton-detected 2D and 3D NMR spectra. FcRn plays a crucial role in regulation of IgG and serum albumin catabolism. It is a clinically validated drug target for the treatment of autoimmune diseases caused by pathogenic antibodies via the inhibition of its interaction with IgG. We herein present the discovery of a small molecule that binds into a conserved cavity of the heterodimeric, extracellular domain composed of an α-chain and β2-microglobulin (β2m) ($FcRn_{ECD}$, 373 residues). X-ray crystallography was used alongside NMR at 100 kHz MAS with sedimented soluble protein to explore possibilities for refining the compound as an allosteric modulator. Proton-detected MAS NMR experiments on fully protonated [^{13}C,^{15}N]-labeled $FcRn_{ECD}$ yielded ligand-induced chemical-shift perturbations (CSPs) for residues in the binding pocket and allosteric changes close to the interface of the two receptor heterodimers present in the asymmetric unit as well as potentially in the albumin interaction site. X-ray structures with and without ligand suggest the need for an optimized ligand to displace the α-chain with respect to β2m, both of which participate in the $FcRn_{ECD}$–IgG interaction site. Our investigation establishes a method to characterize structurally small molecule binding to nondeuterated large proteins by NMR, even in their glycosylated form, which may prove highly valuable for structure-based drug discovery campaigns.

Funding: Deutsche Forschungsgemeinschaft (grant number SFB 1078 B1). The funder had no role in study design, data collection and analysis, decision to publish, or preparation of the manuscript. iNEXT (grant number WP1). The funder had no role in study design, data collection and analysis, decision to publish, or preparation of the manuscript. Swiss National Science Foundation (grant number 200020_159707 and 200020_146757). The funder had no role in study design, data collection and analysis, decision to publish, or preparation of the manuscript. European Research Council (grant number 741863, FASTER). The funder had no role in study design, data collection and analysis, decision to publish, or preparation of the manuscript.

Competing interests: I have read the journal's policy and the authors of this manuscript have the following competing interests. Alex Macpherson, Fabien Lecomte, Richard D. Taylor, Tim Norman, Marta Westwood, Ben Cossins, James White, Robert Griffin, Christine Prosser, Sebastian Kelm, Alistair Henry, Richard Taylor, and Alastair D. Lawson are all current or former employees and/or shareholders in UCB Pharma. Nicolas Basse is an employee and/or shareholder in Sanofi. Hervé Deboves is an employee and/or shareholder in Evotec. John Porter is an employee and/or shareholder in Midatech Pharma. Katharine Cain is an employee and/or shareholder in Vertex. Amy H. Sullivan and David Fox III are/were employees and/or shareholders in Beryllium Discovery. This work was funded by UCB Pharma.

Abbreviations: β2m, β2-microglobulin; APS, Advanced Photon Source; AUC, analytical ultracentrifugation; BMRB, Biological Magnetic Resonance Data Bank; CD8, cluster of differentiation 8; CLS, Canadian Light Source; COOT, Crystallographic Object-Oriented Toolkit; CP, Cross Polarization; CSP, chemical-shift perturbation; ECD, extracellular domain; FcRn, neonatal Fc receptor; $FcRn_{ECD}$, extracellular domain of the neonatal Fc receptor; HSA, Human Serum Albumin; IgG, Immunoglobulin G; MAS, magic-angle-spinning; MHC1, class I major histocompatibility complex; ORF, Open Reading Frame; PDB, Protein Data Bank; r.m.s.d., root mean square deviation; SPR, Surface Plasmon Resonance; TCR, T cell receptor; TIPS, titerless infected-cells preservation and scale-up.

Author summary

In drug design, a detailed characterization of structural changes induced by drug binding is useful for further optimizing lead compounds. In many cases, structural alterations are distant from the compound binding site, potentially acting through allosteric effects. These allosteric effects are often difficult to observe by static methods, i.e., X-ray crystallography, but can be monitored by NMR spectroscopy. The latter method, however, has size-limitations when investigating the protein backbone structure in solution-state. To overcome this, we present an innovative approach employing ultrafast magic-angle-spinning (MAS) NMR on the extracellular domain of the neonatal Fc receptor ($FcRn_{ECD}$). This is a validated drug target in autoimmune diseases, and we aim to identify and characterize novel compounds to serve as starting points to develop allosteric inhibitors of this receptor. After sedimentation, we could record well-resolved proton-detected MAS NMR spectra of the fully protonated [^{13}C,^{15}N]-labeled protein, enabling the observation of structural changes. In combination with computational methods, X-ray crystallography, and other biophysical tools, we present new compounds that may be used as allosteric modulators of FcRn after further optimization. The introduced MAS NMR approach can be applied to a large variety of proteins to support structure-based drug design, facilitating the detection of allosteric effects.

Introduction

In order to discover new chemical drugs, fragment screening followed by structure-based design is an efficient way to sample chemical space and find hits for challenging target classes such as protein-protein interactions [1–3]. In addition to discovering orthosteric ligands, fragment screening has the potential to locate secondary binding sites on a protein that may be exploited for allosteric regulation [4]. In the development process, a methodology that includes detection of allosteric effects is highly welcome. Magic-angle-spinning (MAS) NMR has the potential to contribute via the detection of long-range chemical-shift changes when the investigated protein is too large for solution-state NMR and can even not be deuterated. It is applied here to a soluble 42 kDa construct of the neonatal Fc receptor (FcRn) within a search for allosteric regulators, employing very fast MAS (100 kHz).

FcRn facilitates new-born humoral immunity by regulating Immunoglobulin (IgG) transport across the epithelium [5]. In addition, it has been shown to bind to IgG and Human Serum Albumin (HSA) at nonoverlapping sites in a pH-dependent manner (Fig 1) [6,7]. This allows maintenance of IgG and HSA homeostasis, accounting for the long serum half-life of both proteins [8–11]. At low pH, the interaction of FcRn with IgG occurs through protonation of ionizable residues, located at the CH2–CH3 hinge of the IgG Fc, which produces transient, intermolecular salt bridges with negatively charged residues on FcRn [12]. The interaction of FcRn with IgG and HSA occurs in acidified early endosomes, diverting the proteins from catabolism and carrying them back to the neutral pH environment of the extracellular compartment. At near-neutral pH, the affinity of the interaction decreases, and the complex dissociates [10,13].

Existing as a heterodimer composed of β2-microglobulin (β2m) and a membrane-anchored α-chain (Fig 1), FcRn is homologous to the class I major histocompatibility complex (MHC1) [14]. MHC1 presents antigenic peptide fragments to the T cell receptor (TCR) in complex with cluster of differentiation 8 (CD8) [14]. In contrast, FcRn is not involved in endogenous peptide presentation to the TCR; its peptide-binding groove is closed and nonfunctional [14].

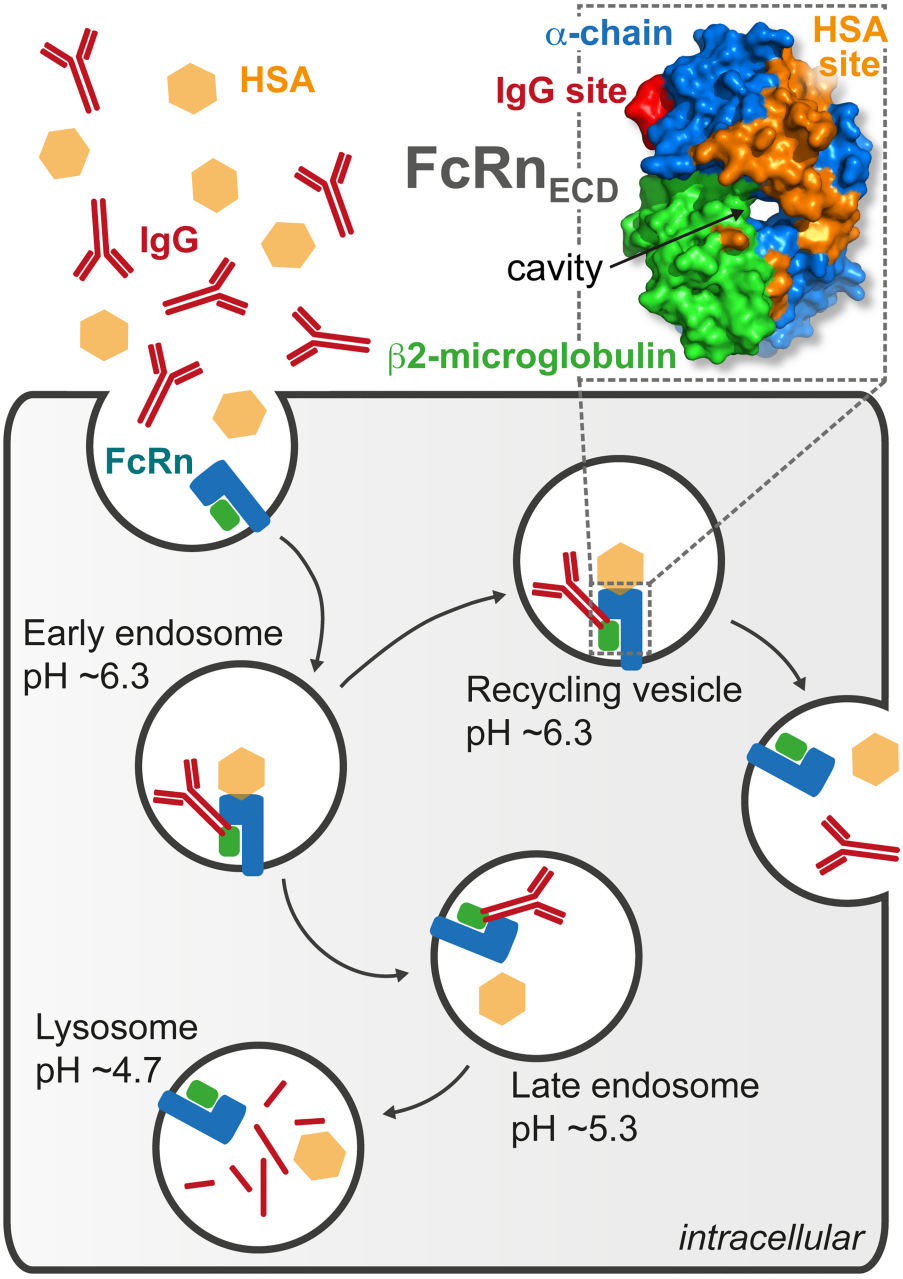

Fig 1. FcRn allows maintenance of protein homeostasis. The soluble extracellular domain of neonatal Fc receptor (FcRn$_{ECD}$, PDB code 1EXU) is a heterodimer composed of β2m (green) and α-chain (blue) with a cavity at the interface between the two proteins. FcRn is involved in the regulation of HSA (orange) and IgG (red) levels. The binding of both HSA and IgG to FcRn is pH dependent, which provides a mechanism for protein homeostasis through endosomal trafficking. β2m, β2-microglobulin; FcRn, neonatal Fc receptor; FcRn$_{ECD}$, extracellular domain of the neonatal Fc receptor; HSA, Human Serum Albumin; IgG, Immunoglobulin G; PDB, Protein Data Bank.

https://doi.org/10.1371/journal.pbio.2006192.g001

The effect of FcRn loss has been studied using β2m-deficient mice, which develop normally but are defective in T cell–mediated cytotoxicity [15]. Deletion of β2m precluded FcRn expression, resulting in a reduction in IgG half-life [16–18]. Additionally, random mutation of residues proximal to the IgG–FcRn binding site allowed selection of Fc variants with increased

affinity for FcRn at pH 6. These Fc constructs maintained pH-dependent binding and showed an extended half-life relative to wild-type IgG [19].

FcRn has been proposed as a drug target in the treatment of autoimmune diseases, in which pathogenic autoantibodies are detrimental to health [20]. Examples of such diseases include, but are not restricted to, myasthenia gravis, Guillain–Barré syndrome, and dermatomyositis [21–24]. Antibodies produced against the FcRn heavy chain ameliorated myasthenia gravis symptoms in rats, and it has been shown that mice without FcRn are resistant to autoimmune disease [25–27]. The current treatment for these conditions is intravenous application of immunoglobulin, which increases the turnover of pathogenic IgG by saturating FcRn [26]. Recently, rozanolixizumab, an antihuman FcRn monoclonal antibody, reduced the serum IgG concentration in a randomized phase 1 study, providing clinical evidence for the potential of an anti-FcRn therapeutic [28].

A chemical inhibitor to control FcRn trafficking is therapeutically desirable for potential treatment of autoimmune disorders. Orthosteric peptide inhibitors with in vivo efficacy have previously been reported [29–33]. Additionally, structure–activity relationships of small molecule antagonists using ELISA assays have also been described [34]. However, to date, no allosteric modulators of FcRn–IgG or FcRn–HSA interactions have been reported. Should such molecules be found, they could be used therapeutically or as tools in biomedical investigations.

In this study, we present the discovery of a compound that binds to the soluble extracellular domain of FcRn, abbreviated here as $FcRn_{ECD}$. In the initial screening process, complementary in silico methods were used to predict binding sites on the basis of charge and topography or sequence conservation, alone and in combination [35–37]. The interaction of the ligand with $FcRn_{ECD}$ is investigated by a combination of X-ray crystallography and proton-detected, ultrafast MAS NMR, revealing its localization in an evolutionarily conserved binding pocket. At high MAS frequencies of 100 kHz, we could acquire well-resolved proton-detected NMR spectra on sedimented, fully protonated $FcRn_{ECD}$, allowing de-novo chemical-shift assignments of residues in the binding pocket and in β2m through establishing sequential connections. MAS NMR pinpoints chemical-shift changes upon ligand binding close to the binding site and in regions distant to it. In this context, MAS NMR helps to exclude the influence of crystal packing effects by making use of protein solutions. Both crystal structures with and without ligand were available, but structural changes were not obvious when using global fitting procedures, with the molecules possibly "locked" into a conformation by crystal contacts. To identify sections of the structure not affected by ligand binding for a fit that is also sensitive to small allosteric effects, residues that did not show chemical-shift changes were used to produce "chemical-shift–informed" overlays of $FcRn_{ECD}$ X-ray structures with and without ligand. Our findings suggest that therapeutic intervention in autoimmune diseases may be achieved through allosteric small molecules that bind to $FcRn_{ECD}$. In addition, such compounds could potentially be used as chemical probes to study FcRn trafficking. The presented approach highlights further the use of MAS NMR for detecting structural changes in nondeuterated proteins expressed in mammalian cells upon ligand binding.

Results and discussion

X-ray crystallography of $FcRn_{ECD}$ and ligandability assessments

Small molecule binding sites on proteins can be identified based on surface shape, charge, and functionality. We used SiteMap software to identify binding sites on the $FcRn_{ECD}$ [35]. To obtain structural data for our analysis, diffraction data for $FcRn_{ECD}$ crystals, at pH 3 and pH 8.5, were collected at cryogenic temperatures and structures solved to 2.0 Å and 2.45 Å, respectively, by molecular replacement. Two copies of $FcRn_{ECD}$ were found in the asymmetric unit.

In addition to the structures at acidic and basic pH, a pH 7.2 structure was generated using molecular dynamics simulation (S1 Fig and S1 Text).

The SiteMap software detected a number of regions with a druggability score >1.0, a nominal quantifier indicating that nM binding might be achieved with a conventional small molecule of <500 Da molecular weight. In particular, SiteMap identified a ligandable site at the interface between the α-chain and β2m (S1 Fig and S1 Text). The respective boundaries were predicted to vary with pH, with the area described as either one large or three distinct cavities.

No regions near the IgG binding site were found by SiteMap. Based on our analysis, should an orthosteric pocket for an IgG blocking small molecule exist, it is likely to be transient in nature and not stabilized in the crystal lattice.

Evolutionary conservation of $FcRn_{ECD}$

On the premise that evolutionarily conserved cavities may have an associated function, we evaluated such conservation of the cavities found by SiteMap (S2 Fig). We identified ortholog sequences using OrthoDB and performed sequence alignments using Clustal Omega [38,39]. A homology model was then created for each sequence using MEDELLER that enabled us to visualize mutations according to the evolutionary conservation in PyMOL [40,41].

Our sequence analysis broadly supports the notion that regions of the protein important for structural integrity or function are conserved, in particular the interface between the α-chain and β2m. It contains key contacts, such as those between $D53_{\beta 2m}$, $Q34_{\alpha\text{-chain}}$, and $S37_{\alpha\text{-chain}}$, and conservation of these contacts preserves the structural integrity of the noncovalently linked heterodimer.

Additionally, motifs within the HSA binding site were also conserved. One of them has previously been identified as being critical for albumin binding and was the site of a protein contact in our pH 3 and pH 8.5 crystal structures, between the two copies of $FcRn_{ECD}$ in the asymmetric unit [8]. We were initially surprised to see the IgG binding site is poorly conserved with the exception of key residues, such as $D130_{\alpha\text{-chain}}$. This may be attributed to the heterogeneity in Fc moieties between mammalian orthologues, which presumably reduces species' cross-reactivity. Of the regions identified by SiteMap, the central cavity was highly conserved, potentially due to the proximity to the dimer interface.

Fragment screening to identify small molecules

Our in silico analysis suggests the presence of an evolutionarily conserved binding site at the interface between the α-chain and β2m. To find ligands for this cavity and, potentially, other sites, a solution-state NMR fragment screen was performed. For this purpose, we used an in-house library of approximately 1,100 molecules containing fluorine atoms to enable ligand interrogation by ^{19}F Carr-Purcell-Meiboom-Gill NMR [42,43]. This screen detected 143 potential binders. In order to select compounds for crystallographic studies, active molecules were further tested in Saturated Transfer Difference NMR experiments and by Surface Plasmon Resonance (SPR), yielding an estimated K_D of 80 μM for the highest affinity fragment, the racemate UCB-FcRn-84 (S3 Fig and S1 Data) [44,45]. Chiral separation showed preferential binding of the R enantiomer. Competition of UCB-FcRn-84 with IgG was tested in a $FcRn_{ECD}$–IgG FRET assay; however, no measurable inhibition was observed.

Crystallographic studies of ligand-bound $FcRn_{ECD}$

Confirmed hits from the fragment-screen were soaked into $FcRn_{ECD}$ crystals that had been grown under acidic conditions. Based on the derived crystal structures, we aimed to further improve both affinity and solubility of the ligand.

UCB-FcRn-84 was found in the conserved cavity at the interface of β2m and the α-chain (S4 Fig and S2 Text), as predicted by SiteMap. Key properties of binding interactions include burial of the 3-fluorophenyl group in a hydrophobic cavity composed of $Y26_{\beta 2m}$, $S52_{\beta 2m}$, $Y63_{\beta 2m}$, $L65_{\beta 2m}$, $W29_{\alpha\text{-chain}}$ and $P228_{\alpha\text{-chain}}$. The most visually striking feature of the binding pocket is a tunnel-like cavity that extends through the middle of the protein (S5 Fig and S2 Text). The bicyclic ring of UCB-FcRn-84 occupies this cavity, being involved in one direct and one water-mediated hydrogen bond to the main-chain of $Q34_{\alpha\text{-chain}}$.

As the fragment was centrally located in this region, it afforded us a tractable chemical platform to explore the binding site further (S4 Fig and S2 Text). We attempted to improve the affinity of UCB-FcRn-84 by better occupying space around the 3-fluorophenyl group, which was nested in a well-defined hydrophobic pocket. Notably, we identified a small area available for growth adjacent to the unsubstituted meta position of the 3-fluorophenyl group. After scanning a range of disubstituted phenyl derivatives, we identified 3,5 difluorophenyl as the best option, yielding a ligand with 2.4 μM affinity for the racemate. Moreover, adding a 3-pyridile group in position 5 led to an equipotent compound (UCB-FcRn-303) but with improved solubility (S5 and S6 Figs, S1 Data and S2 Text).

The crystal structure of UCB-FcRn-303 bound to $FcRn_{ECD}$ displays the R enantiomer (Fig 2 and S5 Fig). The binding mode is consistent with the position observed for UCB-FcRn-84 (Fig 2A and 2B, S4 and S5 Figs). The di-substituted phenyl ring better fills the hydrophobic pocket in the α-chain/β2m interface, while hydrogen bond interactions are maintained with the α-chain and the local water network.

In biochemical experiments molecules from our series did not inhibit IgG binding when tested in a $FcRn_{ECD}$–IgG FRET competition assay. This was consistent with our crystallographic studies which showed no discernible change in the IgG binding site, although accurate interpretation of small changes may be hampered by crystal contacts. The $FcRn_{ECD}$ crystallized with two copies of the heterodimer present in the asymmetric unit, packing in an anti-parallel fashion (Fig 2A). Overlay of the IgG heavy chain–$FcRn_{ECD}$ complex (Protein Data Bank [PDB] code 1FRT) with the ligand-free crystal structure shows significant overlap between CH2 and CH3 domains of IgG and symmetry related copies of $FcRn_{ECD}$ (S7 Fig) [46].

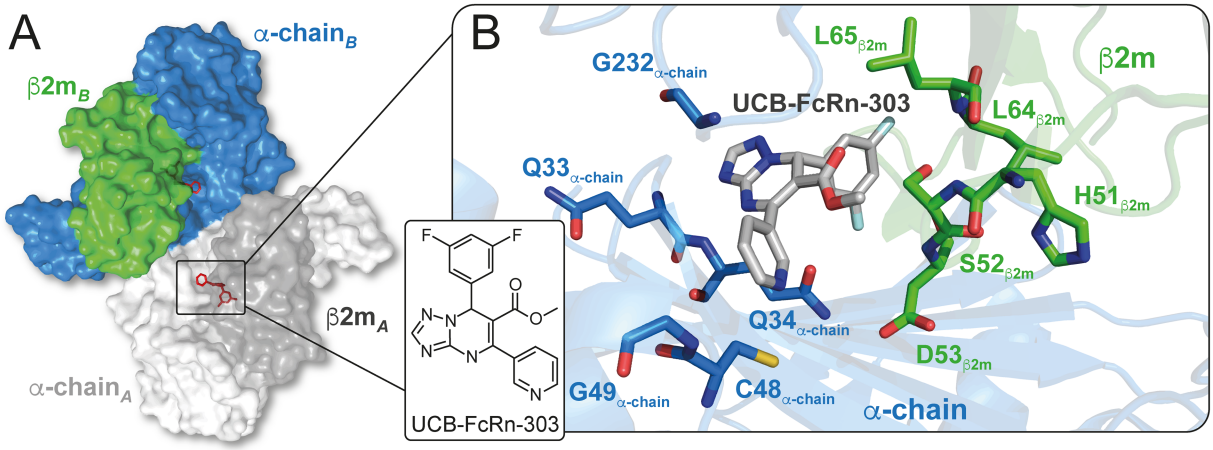

Fig 2. Crystal structure of the compound UCB-FcRn-303 (R enantiomer) bound to $FcRn_{ECD}$. (A) The protein crystallized as a dimer composed of two β2m (dark grey and green) and two α-chain (light grey and blue) molecules. **(B)** At the interface of β2m and the α-chain, UCB-FcRn-303 (grey) occupies a binding pocket with Glycine, Cysteine, hydrophobic (Leucine), charged (Histidine, Aspartate), and polar uncharged (Serine, Glutamine) residues. β2m, β2-microglobulin; FcRn, neonatal Fc receptor; $FcRn_{ECD}$, extracellular domain of the neonatal Fc receptor.

https://doi.org/10.1371/journal.pbio.2006192.g002

In order to determine whether the ligand might induce small conformational and/or dynamic changes in regions beyond the direct binding site, we have used orthogonal solution-based techniques, which will avoid conformational restrictions imposed by crystal packing.

Sedimented, fully protonated $FcRn_{ECD}$ yielded well resolved proton-detected MAS NMR spectra

Until recently, solution-state and proton-detected MAS NMR typically required deuteration of proteins in the size-range of the 42 kDa $FcRn_{ECD}$, as the signal-to-noise ratios obtained in triple-resonance experiments involving $^{13}C\beta$ and $^{13}C\alpha$ chemical-shifts critically depend on the T_2 of ^{13}C coherences [47,48]. Since we were unable to produce deuterated $FcRn_{ECD}$ in sufficient amounts it was not possible to acquire 3D solution-state NMR spectra that would allow sequential assignments. The spectral quality of a 2D ^{15}N-^{1}H correlation spectrum recorded in solution, however, is remarkably high (S8 Fig) [49]. It indicates that $FcRn_{ECD}$ most likely does not form a stable dimer of heterodimers in solution at the applied concentrations, which agrees with biochemical data and earlier studies [50]. At least 227 of the expected 349 backbone amide signals could be observed, with the remainder of the signals most probably obscured by overlap.

To circumvent these experimental limitations, we applied MAS NMR. Progress in recent years, in particular ever faster sample spinning, enables the acquisition of proton-detected MAS NMR spectra on fully protonated samples which increases sensitivity and facilitates resonance assignments through triple-resonance experiments [51–54]. At the highest MAS frequency routinely available (110 kHz), well resolved proton spectra have been reported for fully protonated microcrystalline and membrane proteins, sedimented assemblies and fibrillar proteins [55–57].

In the present case, we have investigated soluble $FcRn_{ECD}$ by MAS NMR experiments via sedimentation. For this purpose, the availability of dedicated filling tools is a prerequisite [58,59]. With the help of such appliances, we sedimented the 42 kDa soluble, fully protonated [^{13}C,^{15}N]-labeled $FcRn_{ECD}$ by ultracentrifugation directly into a 0.7 mm MAS rotor (Fig 3A).

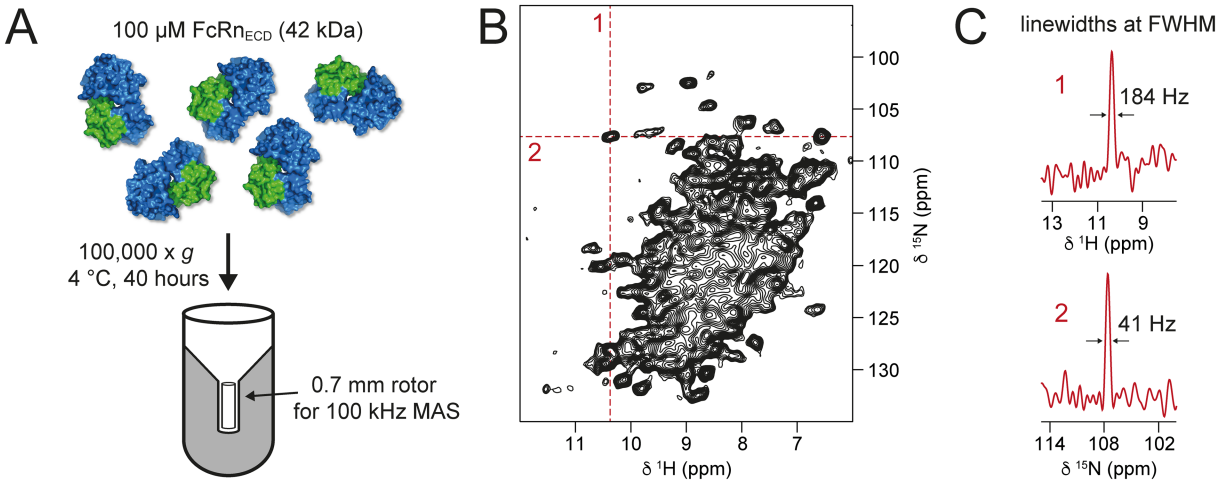

Fig 3. Proton-detected MAS NMR on fully protonated $FcRn_{ECD}$. (A) The soluble $FcRn_{ECD}$ (42 kDa) was sedimented by ultracentrifugation at 100,000 x *g* directly into a 0.7 mm MAS NMR rotor using a home-made filling tool. **(B)** 2D ^{15}N-^{1}H correlation spectrum recorded at 100 kHz MAS of fully protonated [^{13}C,^{15}N]-labeled $FcRn_{ECD}$. **(C)** Typical linewidths of ^{1}H (1) and ^{15}N (2) at full-width-half-maximum (FWHM) of a selected cross peak from the ^{15}N-^{1}H spectrum. β2m, β2-microglobulin; FcRn, neonatal Fc receptor; $FcRn_{ECD}$, extracellular domain of the neonatal Fc receptor.

https://doi.org/10.1371/journal.pbio.2006192.g003

The 2D ^{15}N-^{1}H correlation spectrum measured at 100 kHz MAS is shown in Fig 3B. The observed linewidths demonstrate a remarkable spectral quality by MAS NMR standards (Fig 3C). Recorded at a magnetic field of about 20 T, the ^{1}H and ^{15}N linewidths of a selected typical cross peak are 184 Hz and 41 Hz, respectively. The amide ^{1}H linewidth of $FcRn_{ECD}$ is still higher than is observed in the model protein GB1, by a factor of approximately 1.8, but similar to the precipitated viral capsid coat protein AP205 [60]. The spectrum displays a large number of unresolved signals and a considerable fraction of signals that are well dispersed, both of which may be assigned on the basis of suitable triple-resonance spectra.

In order to monitor the folding state of $FcRn_{ECD}$ in the sedimented sample, we compared the MAS ^{15}N-^{1}H spectrum to the ^{15}N-^{1}H correlation recorded in solution (S8 Fig and S3 Text). The agreement of the spectra indicates that the structure of $FcRn_{ECD}$ in solution is very similar to the one in the sedimented sample. $FcRn_{ECD}$ did not form the stable dimers of heterodimers in solution as had been observed in the crystal structure. Analytical ultracentrifugation, however, reveals a concentration-dependent protomer–diprotomer equilibrium of the $FcRn_{ECD}$ heterodimer in solution, with a very low populated diprotomer fraction (S9 Fig and S4 Text). It is possible that this equilibrium is changed in the sedimentation process which may explain small chemical-shift differences. However, due to the signal overlap in the ^{15}N-^{1}H MAS NMR spectrum, a more detailed chemical-shift comparison is not possible.

Resonance assignments in proton-detected MAS NMR spectra of $FcRn_{ECD}$

To allow interpretation of chemical-shift perturbations (CSPs) upon binding of UCB-FcRn-303 to $FcRn_{ECD}$, resonance assignments are critical. The high MAS frequencies now available facilitate an assignment procedure based on triple-resonance MAS NMR experiments as in solution-state NMR. These include (H)CANH, (H)CBCANH, (H)CA(CO)NH, and (H)CBCA(CO)NH spectra, yielding assignments of ^{15}N, $^{1}H^{N}$, ^{13}Cα0, and ^{13}Cβ chemical-shifts [61,62]. If it is not possible to obtain a (H)CBCA(CO)NH spectrum with sufficient signal-to-noise due to too short ^{13}Cα and ^{13}CO relaxation times, the first two experiments allow for identification of amino acids that, in a following step, can be sequentially connected according to the protein sequence by using a (H)CA(CO)NH spectrum. In this study, such spectra were acquired on the fully protonated [^{13}C,^{15}N]-labeled $FcRn_{ECD}$ enabling assignments of 25 α-chain residues close to the binding pocket and of 73% of all β2m residues.

To ease the assignment of β2m resonances, we made use of data in Beerbaum and colleagues, in which [^{2}H,^{13}C,^{15}N]-labeled β2m was investigated in complex with unlabeled MHC1 [63]. However, the final assignments were achieved by establishing sequential connections along the protein backbone, as shown for the sequence from $K41_{\beta 2m}$ to $R45_{\beta 2m}$ (Fig 4). All chemical-shift assignments are listed in S1 Table and S2 Data and are deposited in the Biological Magnetic Resonance Data Bank (BMRB) (accession number 27437). In total, signals of 98 residues were assigned this way (S1 Table, S2 Data, and S5 Text). The more sensitive (H)CANH spectrum contained 84 additional resolved cross peaks that could not be assigned further due to overlap or lacking correlations in the less sensitive (H)CA(CO)NH and (H)CBCANH spectra.

Interestingly, a large number of the measured ^{13}Cα, ^{13}Cβ, ^{15}N, and ^{1}H chemical-shifts of β2m in the $FcRn_{ECD}$ heterodimer match the observed solution-state NMR resonances for deuterated β2m in MHC1 complexes of the previous study (S1 Table and S5 Text) [63]. Differences in chemical-shifts can be explained by ^{1}H/^{2}H isotope effects, the limited number of amino acid substitutions in MHC1, potential dimers of $FcRn_{ECD}$ heterodimers in the sedimented sample, and differences in buffer and temperature [64]. The similarity of the chemical-shifts supports the notion that β2m adopts its globular fold in the sedimented sample of

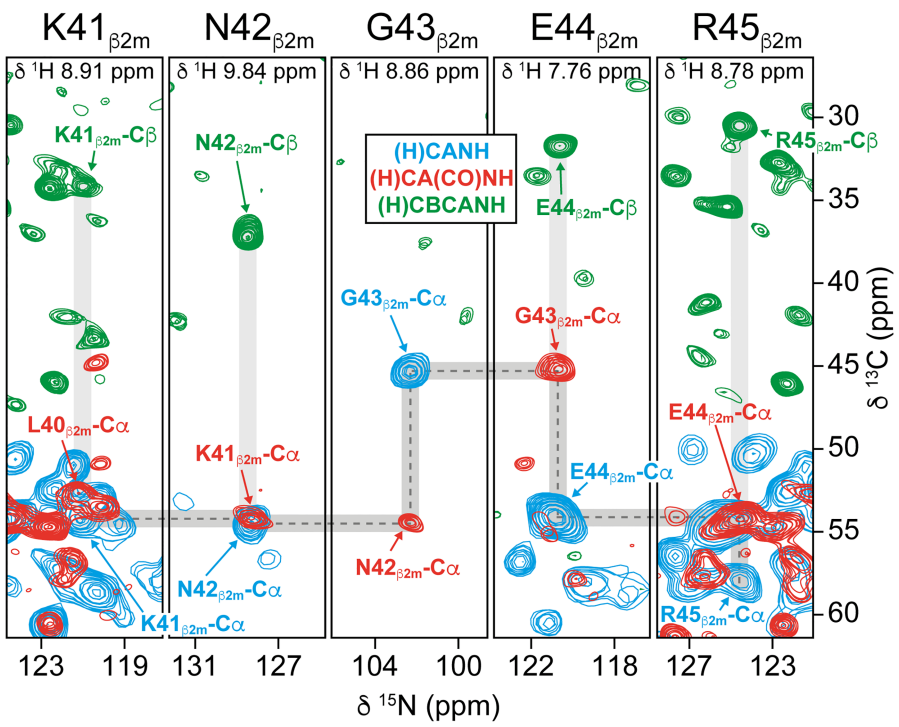

Fig 4. Triple-resonance MAS NMR spectra enable assignments of chemical-shifts. Sequential resonance assignments using the experiments (H)CANH (blue), (H)CA(CO)NH (red), and (H)CBCANH (green) recorded on fully protonated [^{13}C,^{15}N]-labeled FcRn$_{ECD}$ at 100 kHz MAS. As an example, the sequential connections from K41$_{β2m}$ to R45$_{β2m}$ in β2m are indicated by dashed lines. All assigned chemical-shifts can be found in S1 Table, S2 Data, and in the BMRB (accession number 27437). β2m, β2-microglobulin; BMRB, Biological Magnetic Resonance Data Bank; FcRn$_{ECD}$, extracellular domain of the neonatal Fc receptor; MAS, magic-angle-spinning.

https://doi.org/10.1371/journal.pbio.2006192.g004

FcRn$_{ECD}$. Based on these findings and on the similarity between the solution-state ^{15}N-^{1}H and MAS ^{15}N-^{1}H spectra, we assume the overall FcRn$_{ECD}$ structure to be highly similar in solution and in sedimented samples (S8 Fig, S3 Text, S1 Table and S5 Text).

In summary, (H)CANH, (H)CA(CO)NH, and (H)CBCANH spectra represent an acceptable basis for obtaining backbone resonance assignments and allowed us to exploit CSPs as monitors for structural alterations in FcRn$_{ECD}$ upon UCB-FcRn-303 binding.

Structural changes in FcRn$_{ECD}$ upon binding of UCB-FcRn-303

CSPs (Δδ) are probes for both direct effects of ligand binding and concomitant long-range structural changes in receptor proteins that may hint at allosteric effects. Since differences between X-ray structures with and without ligand may be masked by crystal contacts, we analyzed this possibility by comparing 3D (H)CANH spectra recorded on samples of FcRn$_{ECD}$ with and without UCB-FcRn-303 (Fig 5A and 5B). The introduction of a third dimension compared to a 2D ^{15}N-^{1}H correlation leads to better spectral resolution. The observed minimal chemical-shift differences are displayed in Fig 5A. Overall, many of the assigned signals show very similar chemical-shifts in both spectra ($\Delta\delta < 0.02$ ppm, white in Fig 5C and 5D), whereas signals that shift significantly (0.02 ppm $< \Delta\delta <$ 0.03 ppm, cyan; 0.03 ppm $< \Delta\delta <$ 0.04 ppm, marine; 0.04 ppm $< \Delta\delta$, dark blue in Fig 5C and 5D) appear well clustered, suggesting a conformational/dynamic change extending from the ligand binding site. In the following discussions, we consider all residues with $\Delta\delta < 0.02$ ppm as not perturbed. Selected cross peaks of

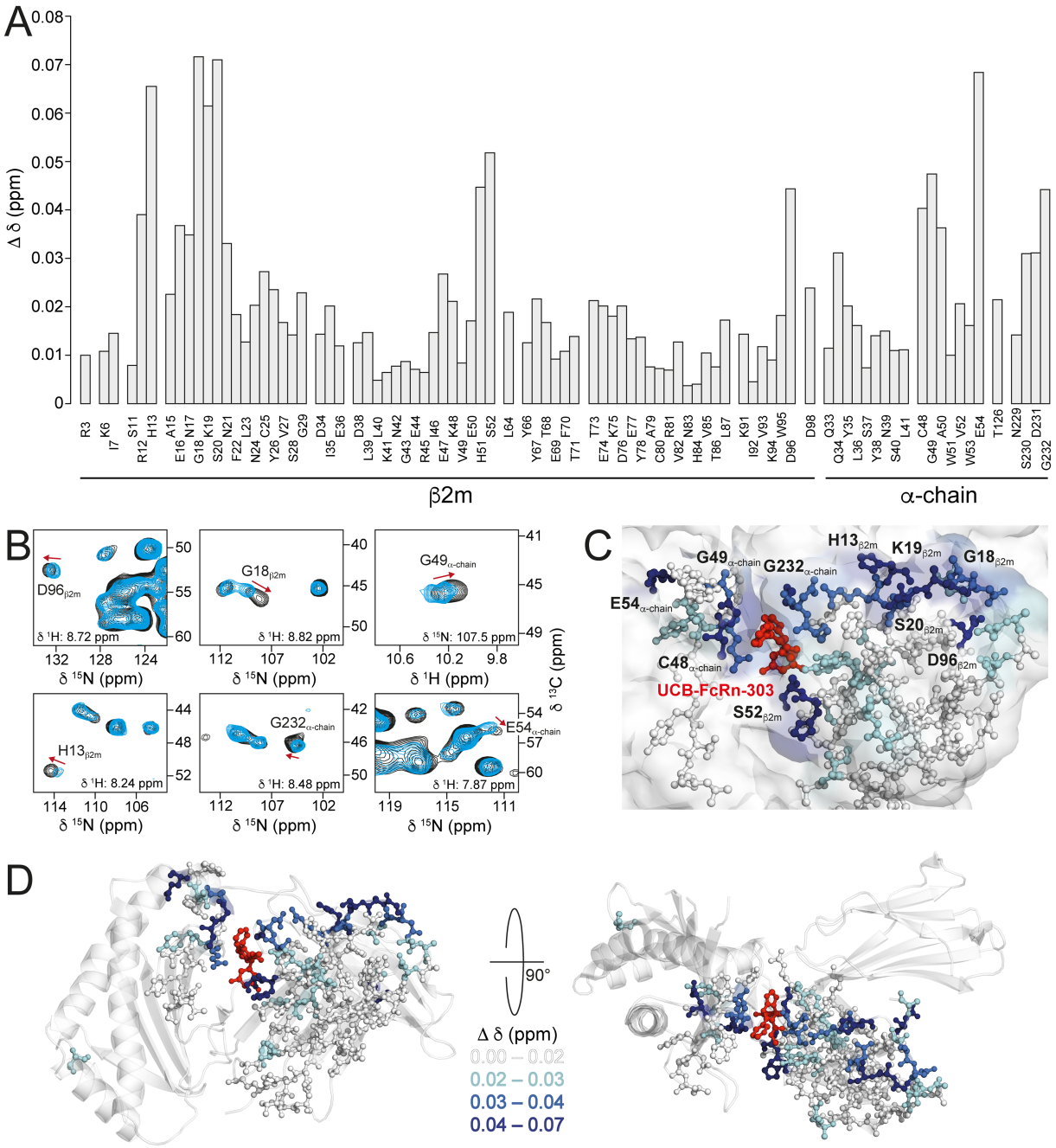

Fig 5. CSPs (Δδ) indicate structural changes in $FcRn_{ECD}$ upon ligand binding. **(A)** CSPs of all assigned amino acids in $FcRn_{ECD}$ upon binding to UCB-FcRn-303, calculated with $\Delta\delta = MIN\{SQRT[(\Delta\delta(^{1}H))^2 + (\Delta\delta(^{13}C)/10)^2 + (\Delta\delta(^{15}N)/5)^2]\}$ (standard deviation = 0.015 ppm). The changes were measured in 3D (H)CANH MAS NMR spectra. **(B)** CSPs upon UCB-FcRn-303 binding to $FcRn_{ECD}$ in 2D planes of 3D (H) CANH spectra with (black) and without (blue) the ligand, both recorded in the presence of 3% DMSO. **(C)** Structural view of UCB-FcRn-303 (red) bound to $FcRn_{ECD}$ with assigned residues in stick representation color-coded according to their CSP ($\Delta\delta < 0.02$, white; $0.02 < \Delta\delta < 0.03$, cyan; $0.03 < \Delta\delta < 0.04$, marine; $0.04 < \Delta\delta$, dark blue). **(D)** Structural view of $FcRn_{ECD}$ in complex with UCB-FcRn-303 (*red*) with the same color-coding of changes in chemical-shifts as in (C). All chemical-shifts can be found in S1 Table, S2 Data, and in the BMRB (accession number 27437). BMRB, Biological Magnetic Resonance Data Bank; CSP, chemical-shift perturbation; FcRn, neonatal Fc receptor; $FcRn_{ECD}$, extracellular domain of the neonatal Fc receptor.

https://doi.org/10.1371/journal.pbio.2006192.g005

strongly affected residues (0.04 ppm < Δδ) are shown in 2D planes of the (H)CANH spectra with and without ligand (Fig 5B). The calculated CSPs shown in Fig 5A are based on the chemical-shift changes in all three spectral dimensions. Large CSPs displayed in Fig 5A may therefore not be obvious from the 2D planes shown in Fig 5B, see $D96_{\beta 2m}$.

As expected, strong effects are seen in the vicinity of the binding pocket of UCB-FcRn-303 observed by X-ray crystallography ($G232_{\alpha\text{-chain}}$, $C48_{\alpha\text{-chain}}$, $G49_{\alpha\text{-chain}}$ and $S52_{\beta 2m}$, Fig 5A and 5C) since the chemical environment of these residues is altered upon binding.

More interestingly, several residues that experienced changes in their chemical-shifts are distant from the binding pocket. These include, for example, $E54_{\alpha\text{-chain}}$ at the C-terminal end of the short α-helix close to the binding region (Fig 5C and 5D). Such an effect could potentially be explained by a small movement of the α-helix. Furthermore, strong CSPs can be observed in a rather remote region composed of loops in β2m, involving $D96_{\beta 2m}$, $G18_{\beta 2m}$, $K19_{\beta 2m}$, $S20_{\beta 2m}$, and $H13_{\beta 2m}$ (Fig 5C and 5D). These residues cluster at the surface close to or at the interface of β2m and the α-chain of two different heterodimers seen in the asymmetric unit (Fig 6A and 6B). A second ligand binding site in this region of $FcRn_{ECD}$ can be excluded since stoichiometric ratios >1 were not observed in SPR experiments or by X-ray crystallography (Fig 2A, S3, S4, S5, S6 Figs, and S1 Data). Interestingly, strong shift changes were observed at comparably long distances from the small molecule binding site. Those strong CSPs may be direct effects of ligand binding, such as introducing a slight displacement of the β2m subunit with respect to the α-chain. Alternatively, it is possible that changes in the protomer–diprotomer equilibrium occur, and thus the chemical-shifts of residues at a potential diprotomer interface are affected. Although we do not observe a stable dimer of heterodimers in solution, a small fraction is present as seen in analytical ultracentrifugation (AUC) experiments (S9 Fig and S4 Text). A diprotomer may also be more highly populated at very high protein concentrations after the applied sedimentation through ultracentrifugation in preparation of 100 kHz MAS experiments. However, the samples with and without ligand have been prepared under identical conditions, making structural effects unrelated to ligand binding unlikely. For a ligand-induced alteration of the equilibrium, long-range structural changes towards the potential diprotomer interface are required, highlighting again the possibility for the occurrence of allosteric effects upon ligand binding.

In the HSA interaction site, a number of strongly affected residues could be found. These included $R12_{\beta 2m}$, $H13_{\beta 2m}$, $C48_{\alpha\text{-chain}}$, $G49_{\alpha\text{-chain}}$, $A50_{\alpha\text{-chain}}$, and $E54_{\alpha\text{-chain}}$ with CSPs around 0.04 ppm or larger (Figs 5A, 6C and S2 Data). Some of these amino acids are close to the binding site of UCB-FcRn-303, but especially $R12_{\beta 2m}$, $H13_{\beta 2m}$, and $E54_{\alpha\text{-chain}}$ are distant to it and may be therefore structurally altered through allosteric effects (Figs 5C and 6C). It is possible that the FcRn–HSA interaction can be modulated with UCB-FcRn-303. The binding site to HSA, however, is located at the possible diprotomer interface and CSPs in this region may be caused by potential ligand-induced changes in the protomer–diprotomer equilibrium of $FcRn_{ECD}$ as discussed above.

Of the NMR assigned residues, only a few from β2m are found in the IgG binding area, such as $R3_{\beta 2m}$ and $T86_{\beta 2m}$ (Fig 6C), for which negligible chemical-shift changes occur (Fig 5A) [46]. In general, residues in the β-sheet region of β2m distant from the binding site or the interface between heterodimers do not exhibit notable CSPs (Fig 5D).

In order to further investigate the potential for allosteric interference with IgG binding, we generated chemical-shift–informed overlays of the two $FcRn_{ECD}$ crystal structures, with and without UCB-FcRn-303. All residues with Δδ < 0.02 ppm (Fig 5A) were used for fitting, including the area around $R3_{\beta 2m}$, $T86_{\beta 2m}$, and $L87_{\beta 2m}$ in β2m that is involved in IgG interaction (Fig 6C), yielding a root mean square deviation (r.m.s.d.) of 0.095 Å. If a movement of the α-helical region of the α-chain could be induced upon ligand binding, it may disseminate

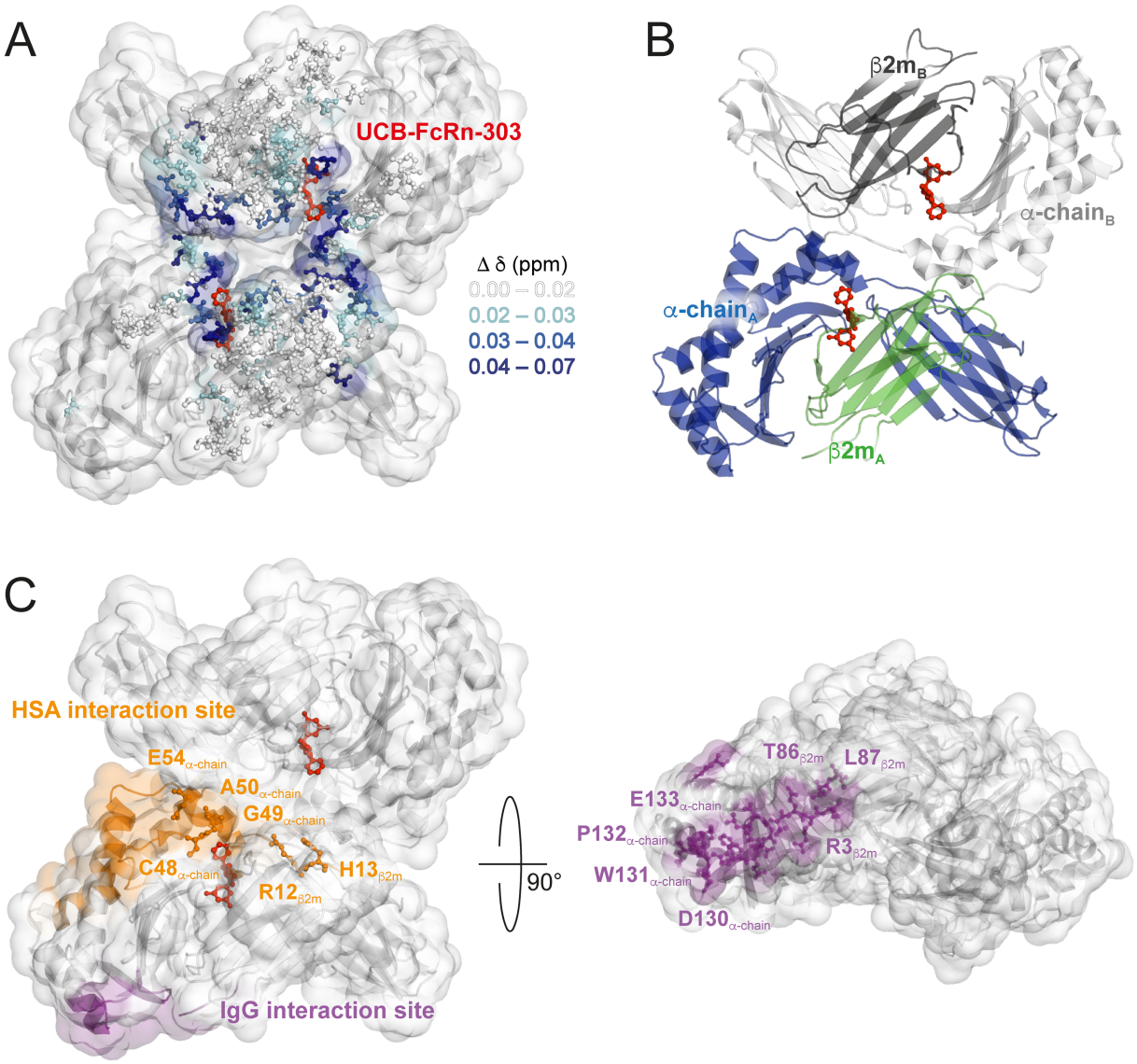

Fig 6. CSPs cluster at the potential $FcRn_{ECD}$ diprotomer interface. (A) CSPs in surface representation of the $FcRn_{ECD}$ diprotomer crystal structure in complex with UCB-FcRn-303 (red), with the same color-coding as in Fig 5. **(B)** For orientation, the $FcRn_{ECD}$ crystal structure is shown in cartoon representation with β2m in green and dark grey and the α-chain molecules in blue and light grey. **(C)** The IgG and HSA interaction sites are depicted in purple and orange, respectively. The highlighted residues are discussed in the text. CSP, chemical-shift perturbation; FcRn, neonatal Fc receptor; $FcRn_{ECD}$, extracellular domain of the neonatal Fc receptor; HSA, Human Serum Albumin; IgG, Immunoglobulin G.

https://doi.org/10.1371/journal.pbio.2006192.g006

towards the loop from $D130_{α\text{-chain}}$ to $E133_{α\text{-chain}}$, which is part of the binding site to IgG (Fig 6C) [46]. Unfortunately, the overlay does not reveal any significant structural changes of α-chain residues close to this loop, except for subtle differences, which we are unable to isolate as a compound-induced effect due to its proximity to crystal packing interactions. Still, the CSPs observed distant to the ligand cavity reveal the potential for allosteric effects in $FcRn_{ECD}$ induced by UCB-FcRn-303 by affecting the HSA interaction site. This provides evidence that binding of an optimized ligand could be aimed at displacing the β2m and α-chain subunits and distally disrupting the IgG binding interface of $FcRn_{ECD}$.

Conclusions

In the context of a druggability study, we identified a compound of <500 Da molecular weight, UCB-FcRn-303, that binds to the extracellular domain of FcRn with low μM affinity. The conserved binding site is located at the interface of β2m and the α-chain, featuring a tunnel-like cavity with solvent access from two different sides. The pocket was identified by computational chemistry methods in a theoretical druggability examination and was corroborated by fragment screening, X-ray crystallography, and NMR spectroscopy. The respective crystal structures show a dimer of heterodimers, with a 1:1 stoichiometry for the ligand/protein complex.

Due to the distance of about 35 Å between the small molecule binding pocket and the site of IgG interaction (Fig 6C), substantial allosteric effects would be required for pharmacologically relevant interference with IgG binding [46]. Such allosteric effects can be monitored by comparing X-ray structures with and without ligand and by NMR spectroscopy via the analysis of ligand-induced CSPs. We therefore established a new approach for testing ligand binding effects on soluble proteins, employing proton-detected 100 kHz MAS NMR spectroscopy on fully protonated $FcRn_{ECD}$. After successful sedimentation of the protein by ultracentrifugation using dedicated filling tools, remarkably well-resolved proton-detected MAS NMR spectra could be obtained and partially assigned. CSPs upon UCB-FcRn-303 binding are observed around the small molecule binding pocket but also distant residues are affected, however, overlapping with the HSA interaction site.

Since a large fraction of residues in β2m towards the IgG binding site and some in the α-chain do not show substantial CSPs (Figs 5A, 6A and 6C), we generated alignments of the two X-ray structures with and without ligand, superposing the nonshifting residues. This approach revealed no substantial changes of residues close to the IgG interaction site upon FcRn-UCB-303 binding, which could modulate the $FcRn_{ECD}$–IgG interaction. It may be envisaged that an optimized ligand could produce a shift of the α-helical region in the α-chain, with potential effects on IgG interaction. Such an optimization could include derivatives with additional functional groups that enter the α-chain/β2m interface and thus produce a slight displacement of the two with respect to each other. Strong CSPs could be observed in the HSA interaction site of $FcRn_{ECD}$, highlighting the potential to achieve a functional modulation of FcRn with UCB-FcRn-303. However, it cannot be fully excluded that changes in oligomeric state of $FcRn_{ECD}$ caused by the ligand under MAS conditions lead to the observed CSPs in this region.

The presented MAS NMR methodology provides an appealing approach for structural investigations of large, soluble proteins expressed in mammalian or other types of eukaryotic cells in which deuteration is challenging, especially in cases when glycosylation is crucial. Moreover, it extends the range of NMR applications to pharmacologically relevant targets, which are often inaccessible by solution-state NMR methods due to size. The MAS NMR approach works with high molecular weight targets and is independent of the physical state of the sample, providing spectral complexity can be handled, e.g., by applying appropriate labelling concepts. This facilitates protein-ligand interaction studies by NMR for any type of protein or biomolecular complex, making previously intractable pharmacological targets accessible, such as the ribosome, G protein-coupled receptors, and the like. Our investigation shows that MAS NMR complements X-ray crystallography in structure-based drug discovery campaigns. It is particularly useful to explore allosteric changes beyond small molecule binding sites, which may be difficult to observe by X-ray crystallography.

Materials and methods

$FcRn_{ECD}$ vector generation

The coding sequences of extracellular domain (ECD) (amino acids 1–297) of human FcRn α-chain and human β2m were synthesized by Entelechon (Entelechon, Regensburg, Germany). The α-chain fragment was cloned into the expression vector pMH (UCB) and the β2m sequence was cloned into pMK (UCB) as HindIII and EcoRI fragments. Both vectors were digested with SalI and NotI and the relevant fragments excised and ligated to generate a vector containing both the α-chain and β2m genes (pM-ECDFcRn-B2M).

The vector was further digested with SalI and a neomycin cassette was ligated in to generate a double gene vector with antibiotic selection (pMFcRnECD-B2M-Neo).

Generation of a $FcRn_{ECD}$ stable mammalian cell line

HEK293 cells were transfected with pMFcRnECD-B2M-Neo using 293fectin (Thermofisher) according to the manufacturer's instructions. Transfected cells were incubated in a static incubator at 37 ˚C and 8% CO_2 for 24 hours. The cells were then diluted to the required concentration with medium supplemented with 0.5 mg/L G418 (Invitrogen) and subsequently divided into 1-mL pools in 24-well plates and incubated in a static incubator at 37 ˚C with 8% CO_2. Every 7 days, the medium was removed from each well and replaced with fresh medium. After a further 14 days, the pools that exhibited cell growth were transferred to 6-well plates. These were expanded up to 50-mL cultures in E250 flasks in shaking incubators. To determine total expression of the $FcRn_{ECD}$ heterodimer composed of β2m and α-chain, batch overgrows were set up and incubated for 10 days.

Samples of the 50-mL batch overgrow supernatants were analyzed for $FcRn_{ECD}$ expression using western blotting. 15 μL of each supernatant was run on a (denatured Tris/Gly gel western blot) alongside known concentrations of purified human FcRn as a control.

The highest expressing pool was expanded (without Neomycin selection) up to 10-L scale in a Wave Bioreactor 20/50 EHT at 37 ˚C, 8% CO_2 for 4 days, at which point the temperature was reduced to 32 ˚C and incubated for a further 6 days. The cell culture was harvested by centrifugation (1,000x *g* for 1 hour) and supernatant put through a 0.22-μm filter.

Purification of $FcRn_{ECD}$ expressed in HEK293 cells

Mammalian cell culture supernatant containing the heterodimer $FcRn_{ECD}$ was concentrated with a 10,000 MWCO membrane using tangential flow filtration (Centramate, Pall) or Amicon stirred cell (Millipore), depending on scale. The sample buffer was exchanged into 50 mM sodium phosphate, pH 5.8, 30 mM NaCl by diluting and concentrating. $FcRn_{ECD}$ was loaded onto a KappaSelect (GE Healthcare) column, which had been preloaded with an IgG4 monoclonal antibody to bind $FcRn_{ECD}$, before washing with 50 mM sodium phosphate, pH 5.8, 30 mM NaCl, and eluting with 50 mM sodium phosphate, pH 8.0, 30 mM NaCl. Elution fractions were analyzed by SDS-PAGE and relevant fractions pooled.

The sample was concentrated using an Amicon spin concentrator (Millipore), 10,000 MWCO membrane. The protein was purified by Gel Filtration with a Superdex 200 (GE Healthcare) column using 25 mM sodium phosphate, pH 7.4, 100 mM NaCl. Peak fractions were analyzed by SDS-PAGE before pooling and concentrating if required.

SPR analysis

SPR was carried out using BIAcore 4000 instruments (GE Healthcare). Reagents including CM5 sensor chips, *N*-hydroxysuccinimide (NHS), *N*-ethyl-*N*-(3-dimethylaminopropyl)

carbodiimide (EDC), and ethanolamine HCl, 10 mM sodium acetate buffers (pH 5.0, pH 4.5) and HBS-P (10x buffer) were obtained from GE Healthcare.

$FcRn_{ECD}$ was diluted into 10 mM sodium acetate buffer, pH 5.0 and immobilized on a CM5 Sensor Chip via amine coupling chemistry to a capture level of approxmimately 4,000 response units. Compounds were screened in a 10-point titration from 200 μM, at 2% DMSO, pH 6.0, and the surface was re-immobilized after each 384-well plate. Injections were performed at a flow rate of 10 μL/min.

All data were double-referenced for blank injections and reference surface, following standard procedures. Both data processing and fitting were performed using Activity Base template protocols developed in house.

Fragment library screening using ^{19}F NMR

A library of approximately 1,100 fluorine-containing fragments were cocktailed into groups of 12 ensuring no overlap of ^{19}F signals. Cocktails were initially prepared at a concentration of 4.2 mM in d6-DMSO and diluted to 800 μM in PBS pH 7.4 before a final dilution to 40 μM ligand concentration (1% d6-DMSO) in either PBS containing 10% D_2O (for control samples) or 20 μM $FcRn_{ECD}$ containing 10% D_2O (for protein samples). NMR spectra were acquired at 25 ˚C on a Bruker 600 MHz AVIII-HD spectrometer equipped with a QCI-F cryoprobe and a SampleJet autosampler. Data were collected using a CPMG pulse sequence with a total echo time of 160 ms across a sweep width of 126 ppm with an acquisition time of 1 s. All spectra were processed using TopSpin 3.2. Fragments were considered binders to $FcRn_{ECD}$ when the ^{19}F signal intensity was significantly reduced in the spectra with $FcRn_{ECD}$ present compared to the spectra recorded in the absence of protein.

Fragment library screening using STD NMR

STD NMR samples were prepared with a ligand to protein ratio of 50:1 (500 μM ligand, 10 μM $FcRn_{ECD}$) in 500 μL phosphate buffered saline, pH 7.4 (90% H_2O, 10% D_2O) with 5% d6-DMSO to help solubilize the ligand. STD NMR spectra were recorded using a Bruker Avance III HD 600 MHz spectrometer equipped with a 5 mm QCI-F Cryoprobe. Data were acquired and processed using the standard Bruker software and were collected at 298 K. The protein was saturated in the methyl region of the spectrum at 0 ppm, and off-resonance saturation was performed at 33 ppm. A series of 120 EBurp2 pulses (50 ms each) were applied with a 4-μs delay between each pulse, resulting in total saturation time of 6 s. Protein signals were removed by applying a spinlock of 100 ms. Interleaved on- and off-resonance data were recorded, processed separately, and then the difference spectra obtained by subtracting the on- from the off-resonance spectra. Data were zero filled once and an exponential multiplication window function applied (LB 2 Hz).

Plasmid construction of $FcRn_{ECD}$ for expression in Sf9 insect cells

The parent construct for α-chain/β2m expresses two Open Reading Frames (ORFs) within one baculovirus multiple-target expression plasmid, pBacugs4X-1. Protein targets are based on the following amino acid sequences (both α-chain and β2m each contain their native leaders): α-chain 1–297 based on NCBI reference sequence NP_004098, β2m 1–119 based on NCBI reference sequence NP_004039. Codons for both ORFs were engineered by GeneComposer for highly expressed baculovirus genes, such that BamHI, HindIII, BglII, and EcoRI restriction sites were eliminated from the inserts to facilitate cloning [65]. Both genes, including flanking restriction sites, were synthesized at GeneArt. The ORF for α-chain was cloned behind the polyhedrin promoter via unique BamHI and HindIII sites; in this case, the BamHI site

preceded the signal sequence while HindIII followed the sequence "TGAT" such that two stops are introduced after the C-terminal residue. The ORF for β2m was cloned behind the p10 promoter via unique BglII and EcoRI sites; the BglII site preceded the signal sequence, while EcoRI followed the sequence "TGATAA" such that two stops are introduced after the C-terminal residue. Using this cloning scheme, polyhedrin and p10 promoters are arranged in divergent/opposing orientations within the baculovirus transfer vector. ORFs were sequence verified prior to the commencement of expression studies.

Expression of $FcRn_{ECD}$ in Sf9 insect cells

The α-chain/β2m construct was transfected into Sf9 insect cells (Expression Systems) using BestBac 2.0, v-cath/chiA Deleted Linearized Baculovirus DNA (Expression Systems, Cat#-91-002). Virus from each transfection was amplified through 3 rounds to produce virus stock for large-scale production. The large-scale preparations were grown in ESF921 medium (Expression Systems, Cat#96–001). Large-scale preparations were infected using the titerless infected-cells preservation and scale-up (TIPS) method [66]. Approximately 10^6 Tni cells (*Trichopulsia ni*, Expression Systems) per mL were infected using 1 mL of TIPS cells. Secreted proteins were harvested after 2–3 days by Tangential Flow Filtration (Spectrum KrosFlo, 0.2 μm filter Cat# P-NO2-E20U-05-N).

Purification of $FcRn_{ECD}$ expressed in Sf9 insect cells

Harvested baculovirus medium (*Trichoplusia ni*) containing secreted $FcRn_{ECD}$ was concentrated 10-fold and buffer exchanged (50 mM sodium phosphate pH 5.8 and 30 mM NaCl via Tangential Flow Filtration (TFF) (Spectrum Labs). The concentrated medium was centrifuged using a JA-10 rotor at 9,000 RPM for 15 minutes at 4 ˚C and then filtered through a 0.2 μm bottle top filter. Three complete EDTA free protease inhibitor tablets were added to the concentrated media prior to chromatography. The filtered concentrated medium was applied to 35 mL of IgG Sepharose FF resin (GE Healthcare) equilibrated with 50 mM sodium phosphate buffer, pH 5.8, and 30 mM NaCl (Sigma) and rotated end over end for one hour at 4 ˚C. The resin was then poured into a gravity flow column and washed with 10 column volumes of the same equilibration buffer. $FcRn_{ECD}$ was eluted from the resin with eight column volumes of 50 mM sodium phosphate buffer pH 8.0 and 30 mM NaCl. The elution fractions containing $FcRn_{ECD}$ were pooled and loaded onto two 5-mL HiTrap Q FF columns (GE Healthcare) and eluted over a 1 M NaCl gradient. The fractions of interest were pooled and glycerol was added to a final concentration of 10%. The pool was concentrated to 15 mg/mL via centrifugal concentration (Amicon Regenerated Cellulose, 10 kDa MWCO, Millipore) and further purified via size exclusion chromatography over a HiLoad 16/600 Superdex 200 pg (GE Healthcare) column in 50 mM HEPES (4-(2-hydroxyethyl)-1-piperazineethanesulfonic acid) pH 7.0 and 75 mM NaCl. The fractions containing $FcRn_{ECD}$ were pooled and concentrated for crystallography via centrifugal concentration (Amicon Regenerated Cellulose, 10 kDa MWCO, Millipore) to 9.9 mg/mL prior to being aliquoted and flash frozen in liquid nitrogen for later use in crystallization experiments.

Crystallization of $FcRn_{ECD}$

In order to search for crystallization conditions for $FcRn_{ECD}$ expressed in insect cells, sitting-drop vapor diffusion crystallization trials were set up at 291 K using a variety of commercial spare-matrix (Rigaku Reagents: JCSG+, Wizard 1/2, Wizard 3/4; Hampton Research: Crystal Screen HTIndex; Molecular Dimensions: PACT, Morpheus, Proplex; Microlytics: MCSG1) using 0.4 μL of protein solution at 5 mg/mL that were mixed with 0.4 μL of reservoir solution

and equilibrated against 80 μL of reservoir solution. The initial crystallization trials produced small kite crystals in several conditions that contain PEG 3350, PEG 6000, or PEG 8000 at low pH. Low pH crystals of $FcRn_{ECD}$ were produced in an optimized crystallization condition screen (Rigaku) containing 12%–16% PEG 6000, 100 mM Citric Acid/Ammonium citrate tribasic pH 3.00–3.09. Crystals of $FcRn_{ECD}$ appeared within 24 hours and grew larger overtime, typically to 50–150 microns in size. The crystals were harvested using 20% glycerol as a cryoprotectant and flash frozen in liquid nitrogen prior to data collection.

Additionally, small rod-like crystals appeared in a single condition at a significantly higher pH (condition PACT H3, 100 mM Bis-Tris Propane/HCl pH 8.5, 200 mM NaI, and 20% PEG 3350) [67]. High/neutral pH crystals of $FcRn_{ECD}$ were produced in optimized crystallization condition containing 100 mM Bis-Tris Propane/HCl pH 8.5, 200 mM NaI, and 20% PEG 3350. Crystals of $FcRn_{ECD}$ appeared within 48 hours and grew larger overtime, typically greater than 150 microns in size. The crystals were harvested using 20% ethylene glycol and flash frozen in liquid nitrogen prior to data collection. To obtain compound bound crystals, apo $FcRn_{ECD}$ crystals grown at pH 3 were soaked for three days in buffer containing 0.1 M Citric Acid/NaOH at pH 3.0, 20% w/v PEG 6000, 20% glycerol, and 12.5–20 mM compound dissolved in 100% DMSO. For crystallization of the UCB-FcRn-303 bound structure of $FcRn_{ECD}$, protein expressed in Sf9 insect cells was used.

Structure determination by X-ray crystallography

Datasets were collected at Canadian Light Source (CLS) on beamline 08ID-1 (CMCF) equipped with a Rayonix MX300 CCD X-ray detector and Advanced Photon Source (APS) on beamline 21-ID-F (LS-CAT) equipped with a Marmosaic 225 CCD X-ray detector. Diffraction data were reduced and scaled with XDS/XSCALE [68]. The structures of $FcRn_{ECD}$ at low and high/neutral pH were solved by molecular replacement using a pre-existing structure of the complex. A significant portion of the structure required remodeling; therefore, Phenix.autobuild was run to generate a starting structure for further refinement. All structures were refined using iterative cycles of TLS and restrained refinement with Phenix.refine and model-building using the Crystallographic Object-Oriented Toolkit (COOT; Version 0.8.1-pre) and were validated using Molprobity prior to deposition in the PDB (IDs 6C97, 6C98, 6C99) [69–73]. Diffraction data and refinement statistics for apo $FcRn_{ECD}$ at pH 3 and both ligand bound structures are listed in S2 Table.

Molecular dynamics simulation

The $FcRn_{ECD}$ structures at pH 3 and pH 8.5 were used as the starting points for molecular dynamics simulation, after adding hydrogen. Protonation states and missing loops were predicted with Maestro (Schrödinger LLC). The structure was solvated in a dodecahedron such that no protein atom was within 10 Å of the edge of the solvent. Monatomic ions were added to a salt concentration of 0.15 M. All simulations were 1,000 ns in length and were carried out with GROMACS 4.6.2 [74]. Particle mesh Ewald was used for long-range electrostatics along with 10 Å cutoffs for Coulomb and Lennard–Jones potential functions.

Expression of fully protonated [^{13}C,^{15}N]-labeled $FcRn_{ECD}$ for NMR experiments

$FcRn_{ECD}$ was expressed using a stable HEK293 cell line, as described above, but the growth media was replaced with Bioexpress 6000 media (Cambridge Isotope Laboratories).

Acquisition of 2D ^{15}N-^{1}H TROSY solution-state NMR spectrum on fully protonated [^{13}C,^{15}N]-labeled $FcRn_{ECD}$

The solution-state 2D ^{15}N-^{1}H TROSY spectrum was acquired from a 0.35-mL sample of 300 μM [^{13}C,^{15}N]-labeled $FcRn_{ECD}$ in a 25 mM Na_2HPO_4, 100 mM NaCl, 50 μM EDTA, 0.02% (w/v) NaN_3 buffer at pH 7.4 containing 5% D_2O/95% H_2O [49]. NMR data were acquired at 35 ˚C on a 600 MHz Bruker AVIII HD spectrometer fitted with a cryogenically cooled probe. The spectrum was acquired for 40 minutes with acquisition times of 40 ms in F_1 (^{15}N) and 60 ms in F_2 (^{1}H). It was processed using Topspin 3.5 (Bruker Biospin Ltd) with linear prediction used to extend the effective acquisition time to 60 ms in F_1.

Sedimentation of $FcRn_{ECD}$ by ultracentrifugation for NMR experiments using fast MAS

A 0.5-mL sample of 100 μM [^{13}C,^{15}N]-labeled $FcRn_{ECD}$ in a 25 mM Na_2HPO_4, 100 mM NaCl, 50 μM EDTA, 0.02% (w/v) NaN_3 buffer at pH 7.4 containing 3% DMSO was directly ultracentrifuged into a 0.7 mm MAS NMR rotor at 100,000 x *g* and 4 ˚C for 40 hours using a swinging bucket ultracentrifuge rotor. Dedicated home-made filling tools were used for this step. Both bottom and top caps of the 0.7 mm MAS rotor were glued to avoid the loss of liquid or removal of caps during MAS. Excess protein and liquid after ultracentrifugation was removed before closing the 0.7 mm NMR MAS rotor. For experiments to detect CSPs, 3 mM UCB-FcRn-303 was added to a 0.5-mL sample of 100 μM [^{13}C,^{15}N]-labeled $FcRn_{ECD}$ in a 25 mM Na_2HPO_4, 100 mM NaCl, 50 μM EDTA, 0.02% (w/v) NaN_3 buffer at pH 7.4 containing 3% DMSO (ligand:protein ratio of 30:1). The ligand-bound sample was sedimented into a second 0.7 mm MAS rotor under the same conditions as the ligand-free sample.

Proton-detected NMR experiments using fast MAS on fully protonated [^{13}C,^{15}N]-labeled $FcRn_{ECD}$

All MAS NMR experiments were performed on a Bruker AVANCE III 850 MHz spectrometer. The spectra were recorded at 80, 90, or 100 kHz MAS with a triple-resonance 0.7 mm MAS probe (Bruker) and referenced to 4,4-dimethyl-4-silapentane-1-sulfonic acid (DSS) (see S3 Table for experimental parameters). The sample temperature of 283 K was monitored by the frequency of the water resonance line. To achieve this sample temperature, the sample was cooled during MAS using nitrogen gas through a cooling unit (BCU II, Bruker) in strong mode with the gas flow set to 400 L/h. (H)NH, (H)CANH, (H)CA(CO)NH, and (H)CBCANH spectra were recorded using Cross Polarization (CP) (heteronuclear transfers) and DREAM (homonuclear transfers) magnetization transfer steps according to the procedures described in Penzel and colleagues [61,75,76]. All spectra were processed with Topspin 3.5 (Bruker) and analyzed with CCPNmr Analysis v. 2.4.2. [77]. All assigned chemical-shifts and observed CSPs are listed in S1 Table and S2 Data, and are deposited in the Biological Magnetic Resonance Data Bank (BMRB) (accession number 27437).

Analytical ultracentrifugation of $FcRn_{ECD}$

Sedimentation velocity experiments were performed at 8 ˚C and 35,000 rpm with an An-60Ti rotor using 12-mm Epon 2-sector centerpieces. For each of the three measurements at different $FcRn_{ECD}$ concentrations (4 μM, 14 μM, and 52 μM), a 400-μL sample in 10 mM Na_2HPO_4, 137 mM NaCl, 2.7 mM KCl, 1.8 mM KH_2PO_4 buffer at pH 7.2 was used. The data were analyzed and plotted with the GUSSI implementation and SEDFIT [78].

Experimental and analytical details for synthetic analogues

All solvents and reagents were used as received from commercial suppliers, unless noted otherwise. The compounds were named using the Biovia Draw 2016 package (IUPAC).

NMR spectra were recorded on a Bruker Avance III HD 500 MHz or 250 MHz spectrometer.

The chemical-shifts (δ) reported are given in parts per million (ppm) and the coupling constants (J) are in Hertz (Hz). The spin multiplicities are reported as s = singlet, d = doublet, t = triplet, q = quartet, dd = doublet of doublet, ddd = doublet of doublet of doublet, dt = doublet of triplet, td = triplet of doublet, and m = multiplet.

uPLC-MS was performed on a Waters Acquity UPLC system coupled to a Waters Acquity PDA detector, an ELS detector and an MSD (Scan Positive: 150–850). Method (pH 3): Phenomenex Kinetix-XB C18 (2.1 x 100 mm, 1.7 μm) column. Elution with a linear gradient of Water + 0.1% Formic acid and Acetonitrile + 0.1% Formic acid at a flow rate of 0.6 mL/min. Chiral SFC analysis: Waters Thar 3100 SFC system connected to Waters 2998 PDA detector, Chiralcel OD-H 25 cm. Chiral SFC separation: Water Thar SFC system with a Waters Thar FDM pump, Waters Thar Alias autoinjector, Waters Thar fraction collector and a Waters 2998 PDA detector.

***(R)* and *(S)* 1-[7-(3-Fluorophenyl)-5-methyl-4,7-dihydro-[1,2,4]triazolo[1,5-a]pyrimidin-6-yl]ethanone (UCB-FcRn-84) (S10 Fig).** 1-[7-(3-fluorophenyl)-5-methyl-4,7-dihydro-[1,2,4]triazolo[1,5-a]pyrimidin-6-yl]ethanone (CAS 691368-95-3) was purchased as a racemate from Life Chemicals and the mixture separated by chiral chromatography using a Chiralpak AD phase (100*500), 300 mL/min with an heptane/isopropanol (8/2) system. 1.21 G of starting material led to respectively 577 mg and 588 mg of separated isomers. Chiral analytical SFC: RT = 8.22 min, 100% ee; RT = 10.40 min, 100% ee.

1-[7-(3,5-Difluorophenyl)-5-methyl-4,7-dihydro-[1,2,4]triazolo[1,5-a]pyrimidin-6-yl] ethanone (S11 Fig). A stirred solution of 3,5-difluorobenzaldehyde (0.1 mL, 0.946 mmol), pentane-2,4-dione (0.146 mL, 1.42 mmol, 1.5 eq.), and *4H*-1,2,4-triazol-3-amine (119 mg, 1.42 mmol, 1.5 eq.) in N,N-dimethylformamide (1.5 mL) was irradiated in a microwave oven (up to 200 W) at 150 ˚C for 60 min. The reaction mixture was left to cool down to ambient temperature and water (6 mL) was added leading to the formation of a precipitate. The resulting solid was collected by filtration, rinsed with water (2 x 1 mL) and cyclohexane (2 x 1 mL), then triturated in hot acetonitrile (1 mL) and dried *in vacuo* to afford 94 mg (34% yield) of the title compound as a pale yellow solid.

The ^{1}H NMR analysis yielded (500 MHz, DMSO-d6) δ 10.89 (s, 1H), 7.70 (s, 1H), 7.14 (t, J = 9.1 Hz, 1H), 6.98 (d, J = 6.3 Hz, 2H), 6.46 (s, 1H), 2.46 (s, 3H), 2.20 (s, 3H). uPLC-MS: $[M+H]^{+}$ m/z = 291, RT = 2.38 min (99%).

***(R)* and *(S)* 1-[7-(3,5-Difluorophenyl)-5-methyl-4,7-dihydro-[1,2,4]triazolo[1,5-a]pyrimidin-6-yl]ethanone (S12 Fig).** The racemate (50 mg) was separated by chiral preparative chromatography on a Chiralpak ASV (50*490) phase, 80 mL/min with a heptane/ethanol (9/1) system to afford 24 mg and 19 mg of the pure enantiomers. Chiral analytical SFC: RT = 10.89 min, 100% ee; RT = 15.16 min, 97.8% ee.

Methyl 7-(3,5-difluorophenyl)-5-(3-pyridyl)-4,7-dihydro-[1,2,4]triazolo[1,5-a]pyrimidine-6-carboxylate (UCB-FcRn-303) (S13 Fig). To a stirred solution of 3,5-difluorobenzaldehyde (150 mg, 1.06 mmol), methyl 3-oxo-3-(pyridin-3-yl)propanoate (265 mg, 1.48 mmol, 1.4 eq.), and *4H*-1,2,4-triazol-3-amine (124 mg, 1.48 mmol, 1.4 eq.) in N,N-dimethylformamide (1.5 mL) was added chloro(trimethyl)silane (0.268 mL, 2.11 mmol) dropwise. The reaction mixture was then irradiated in a microwave oven (up to 200 W) at 130 ˚C for 60 minutes. The reaction mixture was left to cool down to ambient temperature and water (6 mL) was

added leading to the formation of a precipitate. The resulting solid was collected by filtration, rinsed with water (2 x 1 mL) and cyclohexane (2 x 1 mL) then recrystallized from acetonitrile (2 mL) and dried in vacuo to afford 238 mg (59% yield) of the title compound as a pale yellow solid. The ^{1}H NMR analysis yielded (500 MHz, DMSO-d6) δ 11.18 (s, 1H), 8.67–8.61 (m, 2H), 7.92 (dt, J = 7.8, 1.9 Hz, 1H), 7.75 (s, 1H), 7.48 (dd, J = 7.8, 4.9 Hz, 1H), 7.20 (tt, J = 9.2, 2.2 Hz, 1H), 7.16–7.10 (m, 2H), 6.50 (s, 1H), 3.27 (s, 3H). uPLC-MS: $[M+H]^{+}$ m/z = 370, RT = 2.12 min (97%).

Supporting information

S1 Fig. Ligandability assessments on $FcRn_{ECD}$ and predicted small molecule binding sites. At low pH binding sites with the capacity to yield high affinity binding are restricted to the dimer interface, with the region described as either one large or three distinct pockets (pockets A-C). At neutral and basic pH, transient sites arise at the albumin binding site, between the α1 and α2 helices (D), and between the β2m and the α3 domain (E). β2m, β2-microglobulin; $FcRn_{ECD}$, extracellular domain of the neonatal Fc receptor.
(JPG)

S2 Fig. Evolutionary conservation of $FcRn_{ECD}$. (A) The pH 3 structure of the human $FcRn_{ECD}$ heterodimer is colored to illustrate sequence conservation in vertebrate orthologues. Universally conserved residues are colored white; mutated residues are shown in red, with the color intensity indicating the BLOSUM62 score of the worst-matching substitution (darker red = more radical amino acid change away from the human residue). Species included in the analysis are: *Pan troglodytes*, *Gorilla gorilla*, *Pongo pygmaeus*, *Macaca mulatta*, *Callithrix aurita*, *Microcebus murinus*, *Otolemur garnettii*, *Mus musculus*, *Rattus norvegicus*, *Cavia porcellus*, *Oryctolagus cuniculus*, and *Bos taurus*. Mutations occur throughout the α-chain and β2m. Areas of clear conservation include the interface of α-chain and β2m and the central cavity that was detected in the SiteMap analysis. **(B)** For reference, human $FcRn_{ECD}$ from the HSA-bound FcRn structure (PDB code 4N0F) has been colored to highlight residues that constitute the surfaces with the Fc moiety of IgG (magenta) and HSA (orange), the α-chain is shown in green and β2m in cyan. β2m, β2-microglobulin; FcRn, neonatal Fc receptor; $FcRn_{ECD}$, extracellular domain of the neonatal Fc receptor; HSA, Human Serum Albumin; IgG, Immunoglobulin G; PDB, Protein Data Bank.
(TIF)

S3 Fig. UCB-FcRn-84 binds with K_D approximately 80 μM to $FcRn_{ECD}$ as measured by SPR. The numerical values can be found in S1 Data. FcRn, neonatal Fc receptor; $FcRn_{ECD}$, extracellular domain of the neonatal Fc receptor; SPR, Surface Plasmon Resonance.
(TIF)

S4 Fig. Crystal structure of the compound UCB-FcRn-84 bound to $FcRn_{ECD}$. The compound binds at the interface of β2m (green) and the α-chain (blue). Also in this crystal structure, a second heterodimer can be found in the asymmetric unit (grey). β2m, β2-microglobulin; FcRn, neonatal Fc receptor; $FcRn_{ECD}$, extracellular domain of the neonatal Fc receptor.
(JPG)

S5 Fig. Crystal structure of UCB-FcRn-303 bound to $FcRn_{ECD}$. The compound occupies the same binding pocket as UCB-FcRn-84 at the interface of β2m (green) and the α-chain (blue). The binding region is a tunnel-like cavity extending through the protein. Again, a second

heterodimer is found in the crystal structure (depicted in grey). β2m, β2-microglobulin; FcRn, neonatal Fc receptor; $FcRn_{ECD}$, extracellular domain of the neonatal Fc receptor.
(JPG)

S6 Fig. UCB-FcRn-303 binds with K_D = 2.4 μM to $FcRn_{ECD}$ as measured by SPR. The numerical values can be found in S1 Data. FcRn, neonatal Fc receptor; $FcRn_{ECD}$, extracellular domain of the neonatal Fc receptor; SPR, Surface Plasmon Resonance.
(TIF)

S7 Fig. The CH2 and CH3 domains (red) of IgG heavy chain in complex with $FcRn_{ECD}$ (α-chain in blue, β2m in green) (PDB code 1FRT) show overlap with symmetry related copies (dark and medium grey) of ligand-free $FcRn_{ECD}$ (light grey) [46]. β2m, β2-microglobulin; $FcRn_{ECD}$, extracellular domain of the neonatal Fc receptor; IgG, Immunoglobulin G; PDB, Protein Data Bank.
(JPG)

S8 Fig. Comparison of $FcRn_{ECD}$ ^{15}N-^{1}H NMR spectra in solution and after sedimentation. **(A)** 2D ^{15}N-^{1}H correlation using TROSY of fully protonated [^{13}C,^{15}N]-labeled $FcRn_{ECD}$ measured in solution. **(B)** Overlay of the spectrum shown in (A) (orange) with a 2D ^{15}N-^{1}H spectrum of sedimented fully protonated [^{13}C,^{15}N]-labeled $FcRn_{ECD}$ recorded at 100 kHz MAS (black). $FcRn_{ECD}$, extracellular domain of the neonatal Fc receptor; MAS, magic-angle-spinning.
(JPG)

S9 Fig. Analytical ultracentrifugation of $FcRn_{ECD}$. Sedimentation velocity experiments at three different concentrations (52 μM, grey; 14 μM, red; 4 μM, blue) exhibit protein concentration dependent peaks at 3.5 S, 5.1 S, and 5.3 S. $FcRn_{ECD}$, extracellular domain of the neonatal Fc receptor.
(JPG)

S10 Fig. *(R)* and *(S)* 1-[7-(3-Fluorophenyl)-5-methyl-4,7-dihydro-[1,2,4]triazolo[1,5-a]pyrimidin-6-yl]ethanone (UCB-FcRn-84). FcRn, neonatal Fc receptor.
(PDF)

S11 Fig. 1-[7-(3,5-Difluorophenyl)-5-methyl-4,7-dihydro-[1,2,4]triazolo[1,5-a]pyrimidin-6-yl]ethanone.
(PDF)

S12 Fig. *(R)* and *(S)* 1-[7-(3,5-Difluorophenyl)-5-methyl-4,7-dihydro-[1,2,4]triazolo[1,5-a] pyrimidin-6-yl]ethanone.
(PDF)

S13 Fig. Methyl 7-(3,5-difluorophenyl)-5-(3-pyridyl)-4,7-dihydro-[1,2,4]triazolo[1,5-a] pyrimidine-6-carboxylate (UCB-FcRn-303). FcRn, neonatal Fc receptor.
(PDF)

S1 Data. Numerical values of SPR experiments in S3 and S6 Figs.
(XLSX)

S2 Data. Observed chemical-shifts and CSP values of $FcRn_{ECD}$ with and without UCB-FcRn-303 as shown in Fig 5. β2m, β2-microglobulin; CSP, chemical-shift perturbation; FcRn, neonatal Fc receptor; $FcRn_{ECD}$, extracellular domain of the neonatal Fc receptor; MHC1, class I major histocompatibility complex.
(XLSX)

S1 Table. ^{1}H, ^{15}N, $^{13}C\alpha$, and $^{13}C\beta$ chemical-shifts observed in proton-detected NMR experiments at 100 kHz MAS on sedimented fully protonated [^{13}C,^{15}N]-labeled $FcRn_{ECD}$. They are compared to the corresponding chemical-shifts (Beerbaum and colleagues) of [^{2}H,^{13}C,^{15}N]-labeled β2m in MHC1 complexes measured in solution-state NMR [63]. Amino acids of the α-chain are depicted in blue, β2m residues in green. β2m, β2-microglobulin; $FcRn_{ECD}$, extracellular domain of the neonatal Fc receptor; MAS, magic-angle-spinning.
(PDF)

S2 Table. X-ray diffraction data and refinement statistics.
(PDF)

S3 Table. Experimental parameters for proton-detected MAS NMR experiments on fully protonated [^{13}C,^{15}N]-labeled $FcRn_{ECD}$. $FcRn_{ECD}$, extracellular domain of the neonatal Fc receptor; MAS, magic-angle-spinning.
(PDF)

S1 Text. Ligandability assessments on $FcRn_{ECD}$. $FcRn_{ECD}$, extracellular domain of the neonatal Fc receptor.
(PDF)

S2 Text. UCB-FcRn-303 binds in a tunnel-like cavity with low μM affinity. FcRn, neonatal Fc receptor.
(PDF)

S3 Text. $FcRn_{ECD}$ adopts a similar structure in solution and sedimented samples. $FcRn_{ECD}$, extracellular domain of the neonatal Fc receptor.
(PDF)

S4 Text. Analytical ultracentrifugation reveals a small fraction of dimers of heterodimers at higher concentrations of $FcRn_{ECD}$ in solution. $FcRn_{ECD}$, extracellular domain of the neonatal Fc receptor.
(PDF)

S5 Text. Observed chemical-shifts of $FcRn_{ECD}$ in MAS NMR experiments. FcRn, neonatal Fc receptor; MAS, magic-angle-spinning.
(PDF)

Acknowledgments

Excellent technical support by Nils Cremer is kindly acknowledged.

Author Contributions

Conceptualization: Daniel Stöppler, Alex Macpherson, Richard Taylor, Beat H. Meier, Hartmut Oschkinat, Alastair D. Lawson.

Data curation: Daniel Stöppler, Alex Macpherson, Susanne Smith-Penzel, David Fox, III.

Formal analysis: Daniel Stöppler, Alex Macpherson, Nicolas Basse, Lorna C. Waters, David Fox, III, Mark D. Carr, Beat H. Meier, Hartmut Oschkinat.

Funding acquisition: Beat H. Meier, Hartmut Oschkinat, Alastair D. Lawson.

Investigation: Daniel Stöppler, Alex Macpherson, Susanne Smith-Penzel, Nicolas Basse, Fabien Lecomte, Hervé Deboves, Richard D. Taylor, Tim Norman, John Porter, Lorna C. Waters, Marta Westwood, Ben Cossins, Katharine Cain, James White, Robert Griffin,

Christine Prosser, Sebastian Kelm, Amy H. Sullivan, David Fox, III, Mark D. Carr, Alistair Henry, Richard Taylor, Beat H. Meier, Hartmut Oschkinat, Alastair D. Lawson.

Methodology: Daniel Stöppler, Alex Macpherson, Susanne Smith-Penzel, Nicolas Basse, Fabien Lecomte, Hervé Deboves, Richard D. Taylor, Tim Norman, John Porter, Lorna C. Waters, Marta Westwood, Ben Cossins, Katharine Cain, James White, Robert Griffin, Christine Prosser, Sebastian Kelm, Amy H. Sullivan, David Fox, III, Mark D. Carr, Alistair Henry, Richard Taylor, Beat H. Meier, Hartmut Oschkinat, Alastair D. Lawson.

Project administration: Daniel Stöppler, Alex Macpherson, Nicolas Basse, Alistair Henry, Richard Taylor, Hartmut Oschkinat, Alastair D. Lawson.

Supervision: Daniel Stöppler, Alex Macpherson, Nicolas Basse, Alistair Henry, Richard Taylor, Beat H. Meier, Hartmut Oschkinat, Alastair D. Lawson.

Validation: Daniel Stöppler, Alex Macpherson, David Fox, III, Mark D. Carr, Hartmut Oschkinat, Alastair D. Lawson.

Visualization: Daniel Stöppler, Alex Macpherson, Marta Westwood.

Writing – original draft: Daniel Stöppler, Alex Macpherson.

Writing – review & editing: Daniel Stöppler, Alex Macpherson, Susanne Smith-Penzel, Nicolas Basse, Fabien Lecomte, Hervé Deboves, Richard D. Taylor, Tim Norman, John Porter, Lorna C. Waters, Marta Westwood, Ben Cossins, Katharine Cain, James White, Robert Griffin, Christine Prosser, Sebastian Kelm, Amy H. Sullivan, David Fox, III, Mark D. Carr, Alistair Henry, Richard Taylor, Beat H. Meier, Hartmut Oschkinat, Alastair D. Lawson.

References

1. Verdonk ML, Hartshorn MJ. Structure-guided fragment screening for lead discovery. Curr Opin Drug Discov Devel. 2004; 7: 404–410. PMID: 15338949
2. Siegal G, Ab E, Schultz J. Integration of fragment screening and library design. Drug Discov Today. 2007; 12: 1032–1039. https://doi.org/10.1016/j.drudis.2007.08.005 PMID: 18061882
3. Magee TV. Progress in discovery of small-molecule modulators of protein-protein interactions via fragment screening. Bioorg Med Chem Lett. 2015; 25: 2461–2468. https://doi.org/10.1016/j.bmcl.2015.04.089 PMID: 25971770
4. Ludlow RF, Verdonk ML, Saini HK, Tickle IJ, Jhoti H. Detection of secondary binding sites in proteins using fragment screening. Proc Natl Acad Sci USA. 2015; 112: 15910–15915. https://doi.org/10.1073/pnas.1518946112 PMID: 26655740
5. Brambell FW, Hemmings WA, Morris IG. A theoretical model of γ-globulin catabolism. Nature. 1964; 203: 1352–1354. PMID: 14207307
6. Raghavan M, Bonagura VR, Morrison SL, Bjorkman PJ. Analysis of the pH dependence of the neonatal Fc receptor/immunoglobulin G interaction using antibody and receptor variants. Biochemistry. 1995; 34: 14649–14657. PMID: 7578107
7. Raghavan M, Chen MY, Gastinel LN, Bjorkman PJ. Investigation of the interaction between the class I MHC-related Fc receptor and its immunoglobulin G ligand. Immunity. 1994; 1: 303–315. PMID: 7889418
8. Chaudhury C, Mehnaz S, Robinson JM, Hayton WL, Pearl DK, Roopenian DC, et al. The major histocompatibility complex-related Fc receptor for IgG (FcRn) binds albumin and prolongs its lifespan. J Exp Med. 2003; 197: 315–322. https://doi.org/10.1084/jem.20021829 PMID: 12566415
9. Borvak J, Richardson J, Medesan C, Antohe F, Radu C, Simionescu M, et al. Functional expression of the MHC class I-related receptor, FcRn, in endothelial cells of mice. Int Immunol. 1998; 10: 1289–1298. PMID: 9786428
10. Ober RJ, Martinez C, Lai X, Zhou J, Ward ES. Exocytosis of IgG as mediated by the receptor, FcRn: an analysis at the single-molecule level. Proc Natl Acad Sci USA. 2004; 101: 11076–11081. https://doi.org/10.1073/pnas.0402970101 PMID: 15258288

11. Ward ES, Martinez C, Vaccaro C, Zhou J, Tang Q, Ober RJ. From sorting endosomes to exocytosis: association of Rab4 and Rab11 GTPases with the Fc receptor, FcRn, during recycling. Mol Biol Cell. 2005; 16: 2028–2038. https://doi.org/10.1091/mbc.E04-08-0735 PMID: 15689494

12. Kim JK, Tsen MF, Ghetie V, Ward ES. Localization of the site of the murine IgG1 molecule that is involved in binding to the murine intestinal Fc receptor. Eur J Immunol. 1994; 24: 2429–2434. https://doi.org/10.1002/eji.1830241025 PMID: 7925571

13. Ober RJ, Martinez C, Vaccaro C, Zhou J, Ward ES. Visualizing the site and dynamics of IgG salvage by the MHC class I-related receptor, FcRn. J Immunol. 2004; 172: 2021–2029. PMID: 14764666

14. Burmeister WP, Gastinel LN, Simister NE, Blum ML, Bjorkman PJ. Crystal structure at 2.2 A resolution of the MHC-related neonatal Fc receptor. Nature. 1994; 372: 336–343. https://doi.org/10.1038/372336a0 PMID: 7969491

15. Zijlstra M, Bix M, Simister NE, Loring JM, Raulet DH, Jaenisch R. β2-microglobulin deficient mice lack $CD4^{-}8^{+}$ cytolytic T cells. Nature. 1990; 344: 742–746. https://doi.org/10.1038/344742a0 PMID: 2139497

16. Israel EJ, Wilsker DF, Hayes KC, Schoenfeld D, Simister NE. Increased clearance of IgG in mice that lack β2-microglobulin: possible protective role of FcRn. Immunology. 1996; 89: 573–578. PMID: 9014824

17. Ghetie V, Hubbard JG, Kim JK, Tsen MF, Lee Y, Ward ES. Abnormally short serum half-lives of IgG in β2-microglobulin-deficient mice. Eur J Immunol. 1996; 26: 690–696. https://doi.org/10.1002/eji.1830260327 PMID: 8605939

18. Praetor A, Hunziker W. β2-microglobulin is important for cell surface expression and pH-dependent IgG binding of human FcRn. J Cell Sci. 2002; 115: 2389–2397. PMID: 12006623

19. Ghetie V, Popov S, Borvak J, Radu C, Matesoi D, Medesan C, et al. Increasing the serum persistence of an IgG fragment by random mutagenesis. Nat Biotechnol. 1997; 15: 637–640. https://doi.org/10.1038/nbt0797-637 PMID: 9219265

20. Wang Y, Tian Z, Thirumalai D, Zhang X. Neonatal Fc receptor (FcRn): a novel target for therapeutic antibodies and antibody engineering. J Drug Target. 2014; 22: 269–278. https://doi.org/10.3109/1061186X.2013.875030 PMID: 24404896

21. Le Panse R, Berrih-Aknin S. Autoimmune myasthenia gravis: autoantibody mechanisms and new developments on immune regulation. Curr Opin Neurol. 2013; 26: 569–576.

22. Feltkamp TE, van den Berg-Loonen PM, Nijenhuis LE, Engelfriet CP, van Rossum AL, van Loghem JJ, et al. Myasthenia gravis, autoantibodies, and HL-A antigens. Br Med J. 1974; 1: 131–133. PMID: 4544224

23. Israeli E, Agmon-Levin N, Blank M, Chapman J. Shoenfeld Y. Guillain-Barré syndrome—a classical autoimmune disease triggered by infection or vaccination. Clin Rev Allergy Immunol. 2012; 42: 121–130. https://doi.org/10.1007/s12016-010-8213-3 PMID: 20890797

24. Curtis AC, Heckaman JH, Wheeler AH. Study of the autoimmune reaction in dermatomyositis. JAMA. 1961; 178: 571–573. PMID: 13882763

25. Liu L, Garcia AM, Santoro H, Zhang Y, McDonnell K, Dumont J, et al. Amelioration of experimental autoimmune myasthenia gravis in rats by neonatal FcR blockade. J Immunol. 2007; 178: 5390–5398. PMID: 17404325

26. Li N, Zhao M, Hilario-Vargas J, Prisayanh P, Warren S, Diaz LA, et al. Complete FcRn dependence for intravenous Ig therapy in autoimmune skin blistering diseases. J Clin Invest. 2005; 115: 3440–3450. https://doi.org/10.1172/JCI24394 PMID: 16284651

27. Akilesh S, Petkova S, Sproule TJ, Shaffer DJ, Christianson GJ, Roopenian D. The MHC class I-like Fc receptor promotes humorally mediated autoimmune disease. J Clin Invest. 2004; 113: 1328–1333. https://doi.org/10.1172/JCI18838 PMID: 15124024

28. Kiessling P, Lledo-Garcia R, Watanabe S, Langdon G, Tran D, Bari M, et al. The FcRn inhibitor rozanolixizumab reduces human serum IgG concentration: A randomized phase 1 study. Sci Transl Med. 2017; 9: eaan1208.

29. McDonnell KA, Low SC, Hoehn T, Donnelly R, Palmieri H, Fraley C, et al. Synthesis and structure-activity relationships of dimeric peptide antagonists of the human immunoglobulin G-human neonatal Fc receptor (IgG-FcRn) interaction. J Med Chem. 2010; 53: 1587–1596. https://doi.org/10.1021/jm901128z PMID: 20092334

30. Mezo AR, Low SC, Hoehn T, Palmieri H. PEGylation enhances the therapeutic potential of peptide antagonists of the neonatal Fc receptor, FcRn. Bioorg Med Chem Lett. 2011; 21: 6332–6335. https://doi.org/10.1016/j.bmcl.2011.08.111 PMID: 21920737

31. Mezo AR, Sridhar V, Badger J, Sakorafas P, Nienaber V. X-ray crystal structures of monomeric and dimeric peptide inhibitors in complex with the human neonatal Fc receptor, FcRn. J Biol Chem. 2010; 285: 27694–27701. https://doi.org/10.1074/jbc.M110.120667 PMID: 20592032

32. Mezo AR, McDonnell KA, Hehir CAT, Low SC, Palombella VJ, Stattel JM, et al. Reduction of IgG in non-human primates by a peptide antagonist of the neonatal Fc receptor FcRn. Proc Natl Acad Sci USA. 2008; 105: 2337–2342. https://doi.org/10.1073/pnas.0708960105 PMID: 18272495

33. Mezo AR, McDonnell KA, Castro A, Fraley C. Structure-activity relationships of a peptide inhibitor of the human FcRn:human IgG interaction. Bioorg Med Chem. 2008; 16: 6394–6405. https://doi.org/10.1016/j.bmc.2008.05.004 PMID: 18501614

34. Wang Z, Fraley C, Mezo AR. Discovery and structure-activity relationships of small molecules that block the human immunoglobulin G-human neonatal Fc receptor (hIgG-hFcRn) protein-protein interaction. Bioorg Med Chem Lett. 2013; 23: 1253–1256. https://doi.org/10.1016/j.bmcl.2013.01.014 PMID: 23375228

35. Halgren TA. Identifying and characterizing binding sites and assessing druggability. J Chem Inf Model. 2009; 49: 377–389. https://doi.org/10.1021/ci800324m PMID: 19434839

36. Kozakov D, Grove LE, Hall DR, Bohnuud T, Mottarella SE, Luo L, et al. The FTMap family of web servers for determining and characterizing ligand-binding hot spots of proteins. Nat Protoc. 2015; 10: 733–755. https://doi.org/10.1038/nprot.2015.043 PMID: 25855957

37. Capra JA, Laskowski RA, Thornton JM, Singh M, Funkhouser TA. Predicting protein ligand binding sites by combining evolutionary sequence conservation and 3D structure. PLoS Comput Biol. 2009; 5: e1000585. https://doi.org/10.1371/journal.pcbi.1000585 PMID: 19997483

38. Zdobnov EM, Tegenfeldt F, Kuznetsov D, Waterhouse RM, Simão FA, Ioannidis P, et al. OrthoDB v9.1: cataloging evolutionary and functional annotations for animal, fungal, plant, archaeal, bacterial and viral orthologs. Nucleic Acids Res. 2017; 45: 744–749.

39. Sievers F, Wilm A, Dineen D, Gibson TJ, Karplus K, Li W, et al. Fast, scalable generation of high-quality protein multiple sequence alignments using Clustal Omega. Mol Syst Bio. 2011; 7: 1–6.

40. Kelm S, Shi J, Deane CM. MEDELLER: homology-based coordinate generation for membrane proteins. Bioinformatics. 2010; 26: 2833–2840. https://doi.org/10.1093/bioinformatics/btq554 PMID: 20926421

41. Delano WL. The PyMOL molecular graphics system, Version 2.0 Schrödinger, LLC.

42. Carr HY, Purcell EM. Effects of diffusion on free precession in nuclear magnetic resonance experiments. Phys Rev. 1954; 94: 630–638.

43. Meiboom S, Gill D. Modified spin-echo method for measuring nuclear relaxation times. Rev Sci Instrum. 1958; 29: 688–691.

44. Forsén S, Hoffman RA. Study of moderately rapid chemical exchange reactions by means of nuclear magnetic resonance. J Chem Phys. 1963; 39: 2892–2902.

45. Forsén S, Hoffman RA. Exchange rates by nuclear magnetic multiple resonance. III. Exchange reactions in systems with several nonequivalent sites. J Chem Phys. 1964; 40: 1189–1196.

46. Burmeister WP, Huber AH, Bjorkman PJ. Crystal structure of the complex of rat neonatal Fc receptor with Fc. Nature. 1994; 372: 379–383. https://doi.org/10.1038/372379a0 PMID: 7969498

47. Gardner KH, Kay LE. The use of ^{2}H, ^{13}C, ^{15}N multidimensional NMR to study the structure and dynamics of proteins. Annu Rev Biophys Biomol Struct. 1998; 27: 357–406. https://doi.org/10.1146/annurev.biophys.27.1.357 PMID: 9646872

48. Frueh DP. Practical aspects of NMR signal assignment in larger and challenging proteins. Prog Nucl Magn Reson Spectrosc. 2014; 78: 47–75. https://doi.org/10.1016/j.pnmrs.2013.12.001 PMID: 24534088

49. Pervushin K, Riek R, Wider G, Wüthrich K. Attenuated T2 relaxation by mutual cancellation of dipole-dipole coupling and chemical shift anisotropy indicates an avenue to NMR structures of very large biological macromolecules in solution. Proc Natl Acad Sci USA. 1997; 94: 12366–12371. PMID: 9356455

50. Gastinel LN, Simister NE, Bjorkman PJ. Expression and crystallization of a soluble and functional form of an Fc receptor related to class I histocompatibility molecules. Proc Natl Acad Sci USA. 1992; 89: 638–642. PMID: 1530991

51. Zhou DH, Shah G, Cormos M, Mullen C, Sandoz D, Rienstra CM. Proton-detected solid-state NMR spectroscopy of fully protonated proteins at 40 kHz magic-angle spinning. J Am Chem Soc. 2007; 129: 11791–11801. https://doi.org/10.1021/ja073462m PMID: 17725352

52. Linser R, Fink U, Reif B. Proton-detected scalar coupling based assignment strategies in MAS solid-state NMR spectroscopy applied to perdeuterated proteins. J Magn Reson. 2008; 193: 89–93. https://doi.org/10.1016/j.jmr.2008.04.021 PMID: 18462963

53. Zhou DH, Nieuwkoop AJ, Berthold DA, Comellas G, Sperling LJ, Tang M, et al. Solid-state NMR analysis of membrane proteins and protein aggregates by proton detected spectroscopy. J Biomol NMR. 2012; 54: 291–305. https://doi.org/10.1007/s10858-012-9672-z PMID: 22986689

54. Barbet-Massin E, Pell AJ, Retel JS, Andreas LB, Jaudzems K, Franks WT, et al. Rapid proton-detected NMR assignment for proteins with fast magic angle spinning. J Am Chem Soc. 2014; 136: 12489–12497. https://doi.org/10.1021/ja507382j PMID: 25102442

55. Lalli D, Idso MN, Andreas LB, Hussain S, Baxter N, et al. Proton-based structural analysis of a heptahelical transmembrane protein in lipid bilayers. J Am Chem Soc. 2017; 139: 13006–13012. https://doi.org/10.1021/jacs.7b05269 PMID: 28724288

56. Struppe J, Quinn CM, Lu M, Wang M, Hou G, Lu X, et al. Expanding the horizons for structural analysis of fully protonated protein assemblies by NMR spectroscopy at MAS frequencies above 100 kHz. Solid State Nucl Magn Reson. 2017; 87: 117–125. https://doi.org/10.1016/j.ssnmr.2017.07.001 PMID: 28732673

57. Stanek J, Andreas LB, Jaudzems K, Cala D, Lalli D, Bertarello A, et al. NMR spectroscopic assignment of backbone and side-chain protons in fully protonated proteins: microcrystals, sedimented assemblies, and amyloid fibrils. Angew Chem Int Ed. 2016; 55: 15504–15509.

58. Böckmann A, Gardiennet C, Verel R, Hunkeler A, Loquet A, Pintacuda G, et al. Characterization of different water pools in solid-state NMR protein samples. J Biomol NMR. 2009; 45: 319–327. https://doi.org/10.1007/s10858-009-9374-3 PMID: 19779834

59. Gardiennet C, Schütz AK, Hunkeler A, Kunert B, Terradot L, Böckmann A, et al. A sedimented sample of a 59 kDa dodecameric helicase yields high-resolution solid-state NMR spectra. Angew Chem Int Ed. 2012; 51: 7855–7858.

60. Andreas LB, Jaudzems K, Stanek J, Lalli D, Bertarello A, Le Marchand T, et al. Structure of fully protonated proteins by proton-detected magic-angle spinning NMR. Proc Natl Acad Sci USA. 2016; 113: 9187–9192. https://doi.org/10.1073/pnas.1602248113 PMID: 27489348

61. Penzel S, Smith AA, Agarwal V, Hunkeler A, Org ML, Samoson A, et al. Protein resonance assignment at MAS frequencies approaching 100 kHz: a quantitative comparison of J-coupling and dipolar-coupling-based transfer methods. J Biomol NMR. 2015; 63: 165–186. https://doi.org/10.1007/s10858-015-9975-y PMID: 26267840

62. Agarwal V, Penzel S, Szekely K, Cadalbert R, Testori E, Oss A, et al. De novo 3D structure determination from sub-milligram protein samples by solid-state 100 kHz MAS NMR spectroscopy. Angew Chem Int Ed. 2014; 53: 12253–12256.

63. Beerbaum M, Ballaschk M, Erdmann N, Schnick C, Diehl A, Uchanska-Ziegler B, et al. NMR spectroscopy reveals unexpected structural variation at the protein–protein interface in MHC class I molecules. J Biomol NMR. 2013; 57: 167–178. https://doi.org/10.1007/s10858-013-9777-z PMID: 24006098

64. Smith AA, Ravotti F, Testori E, Cadalbert R, Ernst M, Böckmann A, et al. Partially-deuterated samples of HET-s (218–289) fibrils: assignment and deuterium isotope effect. J Biomol NMR. 2017; 67: 109–119. https://doi.org/10.1007/s10858-016-0087-0 PMID: 28074361

65. Lorimer D, Raymond A, Walchli J, Mixon M, Barrow A, Wallace E, et al. Gene Composer: database software for protein construct design, codon engineering, and gene synthesis. BMC Biotechnol. 2009; 9: 36–58. https://doi.org/10.1186/1472-6750-9-36 PMID: 19383142

66. Wasilko DJ, Lee SE, Stutzman-Engwall KJ, Reitz BA, Emmons TL, Mathis KJ, et al. The titerless infected-cells preservation and scale-up (TIPS) method for large-scale production of NO-sensitive human soluble guanylate cyclase (sGC) from insect cells infected with recombinant baculovirus. Protein Expr Purif. 2009; 65: 122–132. https://doi.org/10.1016/j.pep.2009.01.002 PMID: 19174191

67. Newman J, Egan D, Walter TS, Meged R, Berry I, Ben Jelloul M, et al. Towards rationalization of crystallization screening for small- to medium-sized academic laboratories: the PACT/JCSG+ strategy. Acta Cryst Section D. 2005; 61: 1426–1431.

68. Kabsch W. XDS. Acta Cryst Section D. 2010; 66: 125–132.

69. Adams PD, Afonine PV, Bunkoczi G, Chen VB, Davis IW, Echols N, et al. PHENIX: a comprehensive Python-based system for macromolecular structure solution. Acta Cryst Section D. 2010; 66: 213–221.

70. Emsley P, Lohkamp B, Scott WG, Cowtan K. Features and development of Coot. Acta Cryst Section D. 2010; 66: 486–501.

71. Chen VB, Arendall WB, Headd JJ, Keedy DA, Immormino RM, Kapral GJ, et al. MolProbity: all-atom structure validation for macromolecular crystallography. Acta Cryst Section D. 2010; 66: 12–21.

72. Berman H, Henrick K, Nakamura H. Announcing the worldwide protein data bank. Nat Struct Biol. 2003; 10: 980. https://doi.org/10.1038/nsb1203-980 PMID: 14634627

73. Berman HM, Westbrook J, Feng Z, Gilliland G, Bhat TN, Weissig H, et al. The protein data bank. Nucleic Acids Res. 2000; 28: 235–242. PMID: 10592235

74. Van Der Spoel D, Lindahl E, Hess B, Groenhof G, Mark AE, Berendsen HJC. GROMACS: fast, flexible, and free. J Comput Chem. 2005; 26: 1701–1718. https://doi.org/10.1002/jcc.20291 PMID: 16211538

75. Pines A, Gibby MG, Waugh JS. Proton-enhanced nuclear induction spectroscopy: a method for high resolution NMR of dilute spins in solids. J Chem Phys. 1972; 56: 1776–1777.

76. Verel R, Ernst M, Meier BH. Adiabatic dipolar recoupling in solid-state NMR: the DREAM scheme. J Magn Reson. 2001; 150: 81–99. https://doi.org/10.1006/jmre.2001.2310 PMID: 11330986

77. Stevens TJ, Fogh RH, Boucher W, Higman VA, Eisenmenger F, Bardiaux B, et al. A software framework for analysing solid-state MAS NMR data. J Biomol NMR. 2011; 51: 437–447. https://doi.org/10.1007/s10858-011-9569-2 PMID: 21953355

78. Schuck P. Size-distribution analysis of macromolecules by sedimentation velocity ultracentrifugation and Lamm equation modeling. Biophysj. 2000; 78: 1606–1619.